actuators

MDPI

Article

Multidisciplinary Optimization for Weight Saving in a Variable Tapered Span-Morphing Wing Using Composite Materials—Application to the UAS-S4

Mohamed Elelwi [1], Felipe Schiavoni Pinto [1], Ruxandra Mihaela Botez [1,*] and Thien-My Dao [2]

[1] Laboratory of Active Controls, Avionics and AeroServoElasticity LARCASE, ÉTS—École de Technologie Supérieure, 1100 Rue Notre-Dame Ouest, Montréal, QC H3C 1K3, Canada; mohamed.elelwi.1@ens.etsmtl.ca (M.E.); felipe.schiavoni-pinto.1@ens.etsmtl.ca (F.S.P.)

[2] Research Team in Machines, Dynamics, Structures and Processes, ÉTS—École de Technologie Supérieure, 1100 Rue Notre-Dame Ouest, Montréal, QC H3C 1K3, Canada; thien-my.dao@etsmtl.ca

* Correspondence: ruxandra.botez@etsmtl.ca

Abstract: This paper is a follow-up to earlier work on applying multidisciplinary numerical optimization to develop a morphing variable span of a tapered wing (MVSTW) to reduce its weight by using composite materials. This study creates a numerical environment of multidisciplinary optimization by integrating material selection, structural sizing, and topological optimization following aerodynamic optimization results with the aim to assess whether morphing wing optimization is feasible. This sophisticated technology is suggested for developing MVSTWs. As a first step, a problem-specific optimization approach is described for specifying the weight-saving structure of wing components using composite materials. The optimization was performed using several approaches; for example, aerodynamic optimization was performed with CFD and XFLR5 codes, the material selection was conducted using MATLAB code, and sizing and topology optimization was carried out using Altair's OptiStruct and SolidThinking Inspire solvers. The goal of this research is to achieve the MVSTW's structural rigidity standards by minimizing wing components' weight while maximizing stiffness. According to the results of this optimization, the weight of the MVSTW was reduced significantly to 5.5 kg in comparison to the original UAS-S4 wing weight of 6.5kg. The optimization and Finite Element Method results also indicate that the developedmorphing variable span of a tapered wing can complete specified flight missions perfectly and without any mechanical breakdown.

Keywords: morphing variable span of a tapered wing (MVSTW); UAS-S4 multidisciplinary numerical optimization; composite materials; CFD and XFLR5; MATLAB; aerodynamic optimization; sizing and topology optimization; finite element method

Citation: Elelwi, M.; Pinto, F.S.; Botez, R.M.; Dao, T.-M. Multidisciplinary Optimization for Weight Saving in a Variable Tapered Span-Morphing Wing Using Composite Materials—Application to the UAS-S4. *Actuators* **2022**, *11*, 121. https://doi.org/10.3390/act11050121

Academic Editor: Ignazio Dimino

Received: 9 March 2022
Accepted: 22 April 2022
Published: 27 April 2022

1. Introduction

Aluminum alloy is a very well-known material in the aerospace sector due to its ideal strength–weight ratio. The space race in the 1960s introduced new materials and technology, including composite materials. At that time, those materials offered the chance to make airplanes stronger, lighter, and have great potential to reduce fuel consumption and thus be more cost-profitable [1–4].

A composite material is created by combining two or more different materials (reinforcement, fillers, and binder) with varying compositions and substantially different physical and chemical properties. When composite materials are considered, they provide a product with an appearance (and performance) that differs from the individual material components. Composites comprise a solid load-bearing material called reinforcement and softer materials arranged in a matrix. Reinforcement adds stiffness and strength to the structure by augmenting the load support. Composite materials are widely employed in

the industry due to their exceptional resistance to chemicals and to most types of corrosion, as well as to their other interesting properties [5,6].

Their numerous and valuable properties include low density, low weight, unmatched manufacturing and processing capabilities, complicated material bodies that are easily fabricated, their suitability for their use on tiny, as well as very large products, low tooling costs, and their ability to incorporate a suitable surface finish. Composite materials have been used extensively and recently to develop over 50% of aerospace components. The key advantages of composite materials consist of reducing the weight of the components and simplifying their assembly. Composites are used to fabricate a variety of aircraft surfaces, including rudders, spoilers, air-brakes, wing ribs, main wings, and turbine engines [7,8].

The initial wide-ranging applications of fiber-reinforced plastics (FRPs) in aircraft wing development date back to the 1960s, when sailplane designers recognized the advantages of their orthotropic properties and low masses. FRPs enable the optimization of laminate rigidity to meet loading requirements in combination with high stiffness-to-mass and strength-to-mass ratios. Using composites in commercial aircraft wings has since grown steadily, encouraged by advancements in manufacturing technology, such as automatic fiber positioning. The optimization of composites has been a field of study for many years, especially in aeroelasticity areas [9]. Fiber-reinforced composite materials can often provide designers with outstanding potential to achieve a wing structure's desired directional stiffness and aeroelastic behavior by optimizing its fiber directions while minimizing weight penalty and its corresponding high specific strength and stiffness [10].

Unmanned Aerial Vehicles (UAVs) have been in use since the 1950s, but with limitations regarding their operation, autonomy, and feasibility [11,12]. The new wingtip model was developed as part of an international CRIAQ project with the aim of exhibiting the wing upper surface and aileron-morphing capabilities in improving wing tip aerodynamic efficiencies [13,14]. As the technology has improved, composite materials are increasingly being used in advanced design for modern aircraft such as the Bombardier-Series, the Airbus A-380, and the Boeing B-787, as well as for designing UAVs. However, UAVs can afford to have a smaller safety margin on the structural side, as a human pilot is on the ground [3,15,16]. In this context, materials not typically used in the aviation industry, such as polymers and 3D-printed materials, have been incorporated for UAV structural design [17–19]. Composites used in the aviation industry should exhibit high-reliability characteristics, namely a high degree of mechanical, impact, and thermal resistance [20–22].

No matter which design method is used, the sizing design must include optimal thickness allocation of different body components: spars, ribs, stringers, and skin [23]. There exist significant interconnections between these two types of design factors (topology and sizing/layout) that are substantial, especially when skin-buckling metrics are considered. Concurrent optimization of sizing and topology is required to achieve the optimal weight-saving tradeoff; however, significant numerical challenges are presented. Layouts may be optimized using non-gradient optimization methodologies [24,25].

Topology optimization was applied by Airbus in the A380 airplane design project to develop new lightweight surfaces. In particular, the leading-edge ribs and fuselage door intercostals of the Airbus A380 achieved a weight reduction of over 1000 kg per aircraft [26]. Similarly, when developing the wings' leading-edge ribs for the B-787 Dreamliner, Boeing incorporated topology, size, and shape optimization to find their optimum shapes. Due to the combination of various optimization techniques, the weight of the B-787's leading-edge ribs was decreased by 24–45% compared to the B-777 aircraft weight [27,28]. The fundamental objective of this research is to develop and accomplish the most effective solution for developing lightweight components of the variable morphing wing while maintaining optimal mechanical properties compared to the UAS-S4 baseline wing. Estimates were calculated using the UAS-S4 characteristic. Hydra technologies developed and manufactured the UAS-S4 Unmanned Aerial System for military and commercial applications (Figure 1). Table 1 summarizes its general characteristics.

Figure 1. Hydra Technologies UAS-S4 Ehecalt.

Table 1. The characteristics of the UAS-S4.

Geometrical Data	Values
Wing Span	4.2 m
Wing Area	2.3 m^2
Total length	2.5 m
Mean Aerodynamic Chord (MAC)	0.57 m
Empty weight	50 kg
Maximum Take-off Weight (MTOW)	80 kg
Loitering Airspeed	35 knots
Maximum Speed	135 knots
Service Ceiling	15,000 ft
Operational Range	120 km

A telescoping mechanism was proposed as a novel approach for the MVSTW. This strategy adds more difficulties to our work by asking us to pay closer attention to various components' design throughout the optimization process. As a continuation of our previous research, this study is dedicated to the selection and use of composite materials rather than a single material (aluminum Alloy-2024-T3) using STO methods to reduce the wing components' weight. A multidisciplinary optimization approach has been used for adaptive wingspan using advanced composite materials for its performance enhancement.

2. The Optimized MVSTW and Load Distribution—Design Outline

A number of studies conducted in Aerospace Research Centers have proven the advantages of wing shape morphing. The LARCASE has accomplished many investigations of the Unmanned Aerial Systems UAS-S4 and UAS-S45 and other projects. The main objective of these investigations is to improve the aerodynamic performance and enhance green aircraft technology [29,30]. These earlier works investigated the multidisciplinary numerical optimization of MVSTW, which integrated automated numerical analyses of aerodynamics, Finite Element Method, and structure optimizations [31]. Aerodynamic analyses have established that increasing the wing area via the span-morphing technique improved its aerodynamic performance, reduced fuel consumption, and increased flight envelope range [32–34]. Another advantage was the ability to dominate roll control using the asymmetric wingspan mechanism rather than conventional control surfaces [35]. Design engineers face the most significant challenge, which is the structural wing weight penalty. To overcome this challenge, structural optimization is considered the most successful technique for weight minimizing by enhancing the structural design and development of the wing. An optimized reference wing was developed based on multidisciplinary numerical optimization consisting of aerodynamic optimization, the Finite Element Method, and structural optimization (topology and sizing) [31,36]. The aerodynamic optimization

was combined with topology optimization results to allocate the wing components within MVSTW segments [35]. The topology and sizing optimization were then repeated for the entire component set using a single material (aluminum alloy-2024-T) to minimize the wing component weight [31].

2.1. MVSTW Layout and Configurations

A reference wing relies on the concept of telescopic wing techniques. This concept was developed as a result of aerodynamic optimization findings, and it consists of parallel wing segments (swept angle geometrical shape) of the inboard and tapered outboard wings, as shown in Figure 2. To allow the inboard segment to move through the outboard segment, the outboard segment must be designed with an appropriate cavity [35].

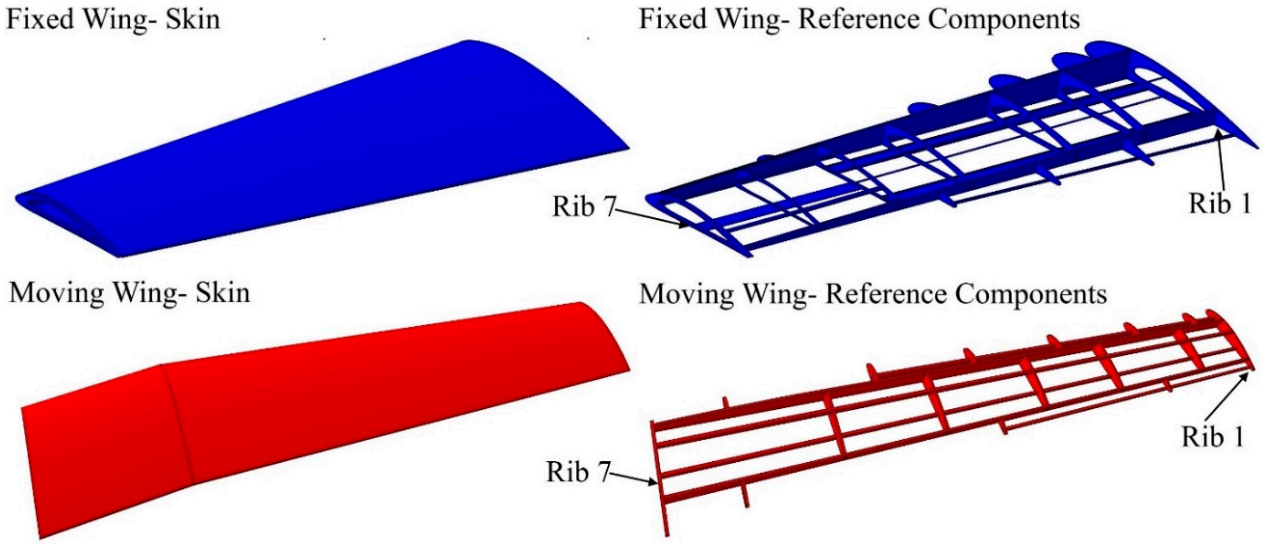

Figure 2. Configuration outline of fixed and moving segments with allocated wing components based on topology optimization.

The previous work [37] concentrated on finding the appropriate location of internal structural components within wing segments. The topology optimization technique was chosen to achieve this objective. This technique has been linked to aerodynamic optimization outcomes and to the data and boundary conditions calculated under extreme situations (sea level altitude and maximum speed, as the maximum pressure was obtained at sea level, and maximum speed when the wingspan was fully extended) [35]. In earlier optimization efforts, a 3 g load factor and a safety factor of 1.5 were used to design a high-strength morphing wing capable of withstanding realistic flight situations such as severe weather (wind shear, thunderstorms, wake turbulence, and others) effects at various altitudes (from sea level to 10,000 ft) [31,37]. According to those topology optimization results, two spars and seven ribs were established within wing segments. The ribs were placed in both segments according to the acquired findings of topology optimization analysis of solid wing segments at the suggested positions, as shown in Figure 2 and Table 2 [37]:

Table 2. Proposed wing rib locations for fixed and moving segments, as measured for reference rib no. 1.

Rib No.	Fixed Wing	Moving Wing
1.	0 mm reference	0 mm reference
2.	269 mm	245 mm
3.	534 mm	626 mm
4.	932 mm	919 mm
5.	1198 mm	1234 mm
6.	1503 mm	1502 mm
7.	1800 mm	1875 mm

2.2. Evaluated Loads along an MVSTW

In the preliminary phase of MVSTW optimization, the lift distribution was calculated along the wingspan, as it is a significant factor in subsequent optimization phases (the first phase was performed on MVSTW optimization with aluminum 2024-T3). The adopted strategy consists of dividing the MVSTW calculation into parts according to the rib positions. The CFD Fluent code was integrated with the XFLR5 code to estimate the flow circulation distribution $\Gamma_{(y)}$. The aerodynamic load was then determined for each MVSTW section using the lifting line theory, as demonstrated in Figure 3 [38].

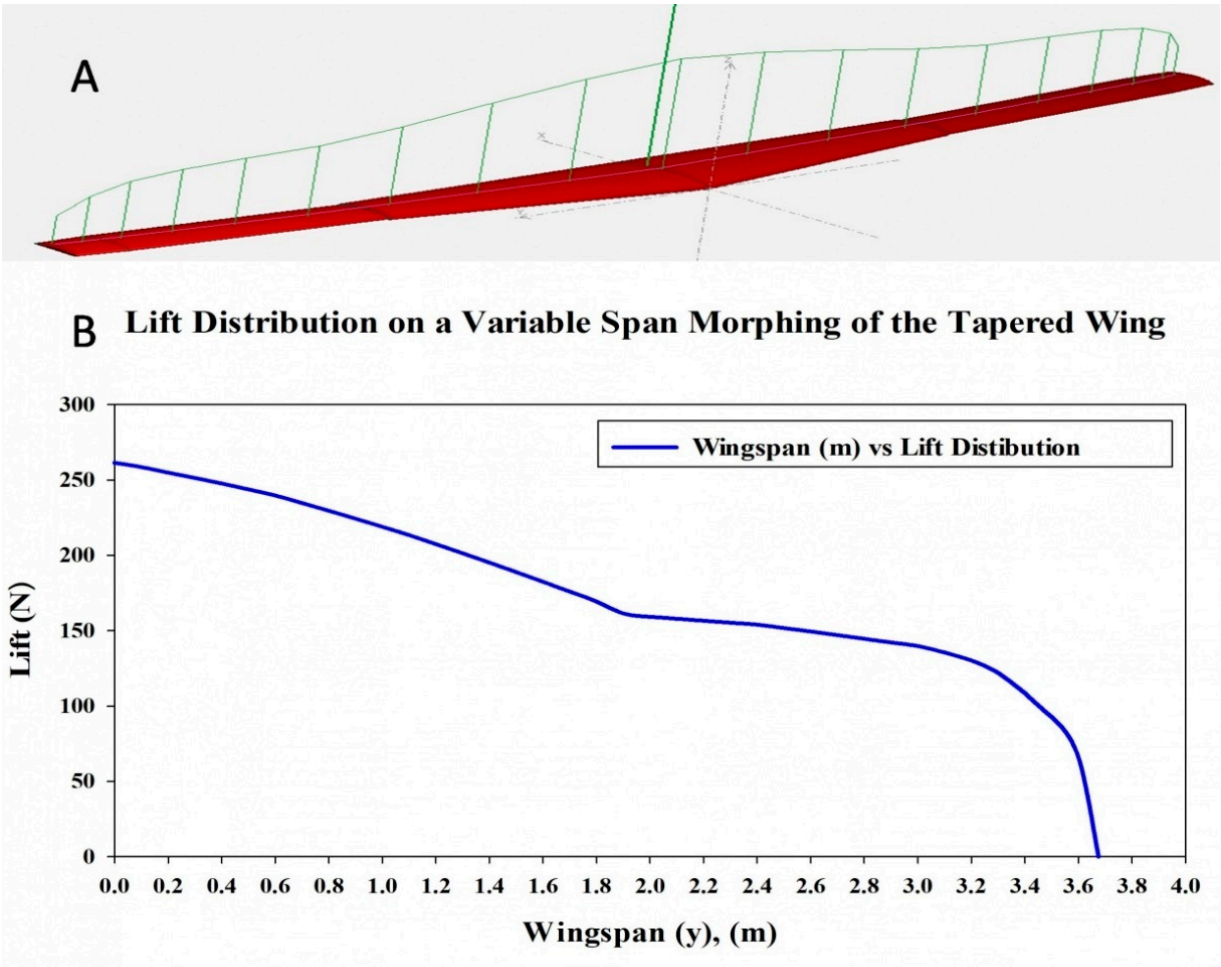

Figure 3. (**A**) Lift distributions for the MVSTW calculated using Fluent XFLR5 code; (**B**) lift force distribution chart.

The Kutta–Joukowski theorem was developed as a way to calculate the distribution of the flow circulation with the following Equations (1)–(3), explained in [39–41].

$$\Gamma_{(y)} = \Gamma_0 \left(1 - \left(\frac{2y}{b}\right)^2\right)^{1/2} \tag{1}$$

In this case, $\Gamma_{(y)}$ denotes the distribution of flow circulation estimated at any random position along the wingspan. $\Gamma_{(y)}$ has its maximum value when $y = 0$, and it tends to zero when $y = \pm b/2$. Thus, the flow circulation in the mid-span of the wing Γ_0 can be calculated as follows:

$$\Gamma_0 = \frac{4L}{\rho V b \pi} \tag{2}$$

where L is the lift force, ρ is the air density, and V represents the air velocity. The following equation can be used to determine the lift loads acting on each wing segment:

$$L_{(y)} = \rho V \Gamma_{(y)} \tag{3}$$

As following the initial topology optimization, the number and type of wing components and their positions were determined. Each wing segment was designed with two spars, seven ribs, and several support components that were developed from the earlier optimization process, as seen in Figure 2 [37]. Al 2024-T3 was selected for all components during the following topology optimization process to reduce the wing structures' weight. The lifting load along the wingspan can be effectively estimated for each segment and it was calculated using the Prandtl lifting-line theory. The main parameters of the wing's span and ribs could then be determined. As shown in Figure 2, the initial topology optimization recommended the positioning of the seven ribs within the moving wing and fixed wing segments in the suggested locations [37]. The MVSTW was divided into 11 separate parts according to the locations of the ribs (each wing segment has 7 ribs) when the wingspan was extended to 75% of the original length of the wing, as depicted in Figure 4.

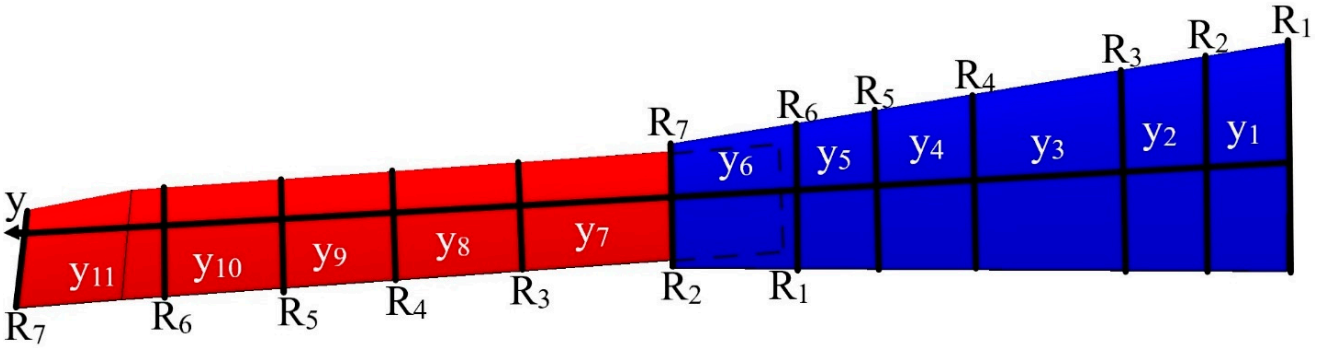

Figure 4. General scheme of an MVSTW with span sections (y_n) and chord numbers].

As stated above, for a reliable and strong wing, the modeling of its structural components included a load factor of 3 g and a safety factor of 1.5. The safety factor of 1.5 was based on the FAA regulations (FAR 25.303). These regulations require aircraft structures to endure appropriate static loads determined by their related aerodynamic pressures without structural damage or failure. [42]. The average lift loads measured for the fixed parts were used to evaluate the fixed wing ribs. The moving segment was treated similarly, with its lift load values shown in Table 3 for that segment [16,31].

Table 3. Lifting loads computed for each section of an MVSTW.

Section Number	Lift Load (N)	Ultimate Load
y1	257.36	1158.1
y2	243.77	1096.97
y3	232.15	1044.65
y4	213.325	959.96
y5	198.29	892.28
y6	175.96	791.8
y7	158.62	713.77
y8	152.7	687.15
y9	147.12	662.04
y10	134.61	605.75
y11	79.11	355.995

3. The Mathematical Approach to the Selection of Composite Materials

A MATLAB algorithm was developed to analyze the final analytical properties of composite materials based on fiber and matrix mechanical characteristics. The lamina longitudinal Young's modulus (E_1), for example, can be determined by the rule of mixtures, where E_{f1} and E_m represent the longitudinal Young's modulus of the fiber and the matrix, respectively, and v_f and v_m are the volume fractions of the fiber and the matrix, respectively.

$$E_1 = E_{f1} * v_f + E_m * v_m \tag{4}$$

where E_{f2} represents the transversal Young's modulus of the fiber.

The transverse Young's modulus (E_2) of a material can be calculated using a variety of methods. The Halpin–Tsai approach is applied in this research, a well-known method with reliable results [43].

$$E_2 = E_m \left(\frac{1 + 2 * \left(\frac{\frac{E_{f2}}{E_m} - 1}{\frac{E_{f2}}{E_m} + 2} \right) * v_f}{1 - \left(\frac{\frac{E_{f2}}{E_m} - 1}{\frac{E_{f2}}{E_m} + 2} \right) * v_f} \right) \tag{5}$$

MATLAB code was used to analyze a simplified load case, for which the equivalent laminate characteristics were determined. This case only considers a single axial load, for which E_x and E_y are determined. A more accurate result can be obtained by developing the full equation by considering the loads per unit length in all directions, a process that can be performed iteratively. The laminate-equivalent properties were determined using for the load case by inverting the laminate stiffness matrix E, which is composed of three other matrices: A, B, and D, representing the laminate extension stiffness, laminate coupling stiffness, and laminate bending stiffness matrices, respectively [44].

$$[E] = \begin{bmatrix} [A] & [B] \\ [B] & [D] \end{bmatrix} \tag{6}$$

$$A_{ij} = \int_{-\frac{t}{2}}^{\frac{t}{2}} \left(\overline{Q}_{ij} \right)_k dz = \sum_{k=1}^{N} \left(\overline{Q}_{ij} \right)_k (z_k - z_{k-1}) \tag{7}$$

$$B_{ij} = \int_{-\frac{t}{2}}^{\frac{t}{2}} \left(\overline{Q}_{ij} \right)_k z dz = \sum_{k=1}^{N} \left(\overline{Q}_{ij} \right)_k \left(z_k^2 - z_{k-1}^2 \right) \tag{8}$$

$$D_{ij} = \int_{-t/2}^{t/2} \left(\overline{Q}_{ij} \right)_k z^2 dz = \sum_{k=1}^{N} \left(\overline{Q}_{ij} \right)_k \left(z_k^3 - z_{k-1}^3 \right) \tag{9}$$

Equations (6)–(9) are functions of the transformed lamina stiffness matrix $\overline{Q}$, and of the distance of each layer (k) from the middle surface (z_k).

The inverted laminate stiffness matrix E is written under the following form:

$$[E]^{-1} = \begin{bmatrix} A' & B' \\ C' & D' \end{bmatrix} \tag{10}$$

The laminate equivalent longitudinal Young's modulus (E_x), transversal Young's modulus (E_y), shear modulus (G_{xy}) and Poisson's ratio (ν_{xy}) are written as follows:

$$E_x = \frac{1}{t\ A'_{11}} \tag{11}$$

$$E_y = \frac{1}{t\ A'_{22}} \tag{12}$$

$$G_{xy} = \frac{1}{tA'_{66}} \tag{13}$$

$$\nu_{xy} = -\frac{A'_{12}}{A'_{11}} \tag{14}$$

where t is the laminate thickness.

The MATLAB code has been used to calculate the appropriate composite materials for output equal each wing component type, including its wing skin, spars, ribs, and support components.

4. Optimization Techniques of the MVSTW

Optimization techniques are receiving increased attention in the aviation field because they are considered the most effective approaches for decreasing a structure's weight while increasing its global stiffness [45]. The topology optimization was performed using the SolidThinking Inspire software, while the sizing optimization was performed using the HyperMesh (OptiStruct) software. The Inspire and OptiStruct codes were designed using the (Solid Isotropic Material with Penalization) SIMP method [46].

The wing elements' structural configuration weight can be minimized by enhancing the wing structure's overall strength and integrity via the application of sizing and topology optimization (STO) [47].

This paper offers a new multidisciplinary optimization (MDO) framework based on design parameters for modeling and analyzing wing elements. It integrates several optimization methods into multiple-computer-aided engineering software. The Sizing and Topology Optimization STO techniques were coupled with the aerodynamic optimization utilizing Computational Fluid Dynamics (CFD) via ANSYS FLUENT and XFLR5 codes.

The fundamental concept behind this investigation is to perform MDO on a composite morphing wing using different composite materials rather than a single metal material (such as aluminum alloy 2024-T3 in [31,37]). The Finite Element Method (FEM) integrates with the STO into an optimization solver.

The multidisciplinary design optimization MDO was used to determine the appropriate composite materials (and their composition) for a morphing wing based on MATLAB calculations. Then, the STO was applied to the selected materials for the design of lightweight wing elements of a morphing wing while improving its mechanical characteristics. The structural and aerodynamic performance of the wing were evaluated using wing parameters that serve as optimization objectives and constraints. STO results based on the selected composite materials were obtained for all wing components; these components were then tested to validate their mechanical properties (displacement, factor safety, and stresses).

4.1. Theoretical Background of the Optimization Technique

Topology Optimization (TO) is a mathematical approach for identifying the optimal material distribution while minimizing its compliance within a predetermined design field. This optimized material configuration can be obtained because the critical material for the structural design is preserved while the undesirable material is removed. Thus, the outcome leads to the best structural load distribution under given boundary conditions and constraints. The TO approach via numerical solvers respects the predetermined constraints while meeting certain objectives. Hence, substantial materials are considered solid, whereas null materials are considered void. A commercial optimization numerical solver is utilized to cope with a set of constraints while relying on the objective functions for determining individual load situations. Sizing and topological optimizations have been implemented using Altair's OptiStruct and SolidThinking's Inspire. The design constraints were addressed within the solvers to ensure that the design requirements were met. As a result, the primary objective of minimizing compliance while maximizing structural stiffness was satisfied.

Wing components are subjected to the design's pre-set loads and parameters to accommodate the density distribution of the material and its other mechanical characteristics (displacements, stresses, and others). Thus, the material density is considered to be the objective function variable, which determines whether a finite element is solid or void. The equations are elaborated on below.

The ith element's pseudo-density, x_i, may range between 0 and 1, i.e., ($0 \leq x_i \leq 1$), where the 0 value indicates void material and the 1 value represents solid material. The variable denoted by the pseudo-density can be defined in Equation (15):

$$x_i = \frac{\rho_i}{\rho_0} \tag{15}$$

where x_i denotes the pseudo-density of the ith element, ρ_i represents the density of the ith element, and ρ_0 indicates the density of the base material. According to the SIMP approach, Equation (16) illustrates the effect of the pseudo-density variable on the material stiffness [48]:

$$E_{(x_i)} = E_{solid}(x_i)^p \tag{16}$$

where E_{solid} stands for the isotropic property of the base material, while superscript p stands for the penalty parameter's exponent. Equation (17) can then be applied to link Young's modulus for (solid and void domains) with the pseudo-density.

$$E_{(x_i)} = E_{void} + x_i{}^p(E_{solid} + E_{void}) \qquad p \geq 1 \tag{17}$$

where Young's modulus E_{void} is assigned to the void area, E_{solid} is assigned to the solid area, and each element's Young's modulus is assigned by $E_{(xi)}$.

The penalty parameter p should be greater than 1 ($p \geq 3$ commonly defined) so that when it is included in the pseudo-density, which impacts the volume constraint while penalizing intermediate densities, there is a significant effect on the TO, as when the density ρ_i approaches 0, the stiffness also approaches 0. As a result, the material is considered as unnecessary and can be regarded as void. By contrast, when the intermediate density approaches 1, the material becomes crucial to the structural integrity and can be regarded to be solid [49].

The TO method's constraint is the volume fraction of the total volume of the designable region as a function of the pseudo-density, as stated in the following equation:

$$V = \sum_{i=1}^{n} x_i V_i \tag{18}$$

where V is the total volume of the designable region and V_i indicates the volume of the ith element.

The objective function is defined to minimize the design structure's compliance while maximizing its stiffness that meets the requirements under the given constraints. The objective function can be mathematically represented as follows:

$$\begin{gathered} \min_x : c(x) = U^T K U = \sum_{e=1}^{N} (x_i)^P u_e^T k_0 u_e \\ \text{subject to} : \frac{V(x)}{V_0} = f \\ : KU = F \\ : 0 < x_{min} \leq x_i \leq 1 \end{gathered} \tag{19}$$

where x represents the variable vector function in the formulation of $c(x)$, the volume fraction is expressed as $\frac{V(x)}{V_0} = f$, where V is the total volume and V_0 is the initial volume, K represents the global stiffness matrix, and U denotes the global displacement; thus, KU equals the force vector F. The displacement vector is u_e, while k_0 denotes the elemental stiffness matrix.

The following constraints must be satisfied during each optimization iteration: the target mass constraint, the global force-stiffness equilibrium, and the requisite functional constraints. Equation (20) expresses how the optimization respects the target mass constraint:

$$\sum_{e=1}^{N} (v_x)^T x_i \leq M_{target} \tag{20}$$

where M_{target} denotes the optimization's target mass.

In a mathematical TO, the density filter shape described by Sigmund is chosen [50,51]. The physical relative density filtration can be determined by $\widetilde{x}_i$, as follows.

$$\widetilde{x}_i = \frac{\sum_{j \in \mathbb{N}_e} w(r_i) v_j \widetilde{x}_j}{\sum_{j \in \mathbb{N}_e} w(r_i) v_j} \tag{21}$$

The following formula expresses a neighborhood setting $N_e = \{i \| r_i - r_e \| \leq R\}$, where R is the filter radius. The filter radii r_i and r_e are defined as those surrounding the centers of elements i and e, respectively. Additionally, the weighting function is denoted by the formula $w(r_i, r_e) = R - \|r_i - r_e\|$, where v_i denotes the volume of the ith element.

Following our previous investigation [31], the main objective in this stage is to apply the optimization to optimized composite materials chosen according to established criteria. Given that the STO has been used to minimize the structural compliance while maximizing the global stiffness under given loads, the wing components' weight has been reduced to produce a lighter morphing weight.

The compliance optimization problem that we considered is formulated in the following equation:

$$C = \int_V f u dV + \int_S t u dS + \sum_i^n F_i u_i \tag{22}$$

where V represents the continuum's volume, f is the distributed body force, t is the traction force, F_i is the point load on the ith node, u is the displacement area, u_i is the ith displacement degree of freedom, and S represents the surface area of the continuum.

4.2. Formulation of the Topology Optimization Objective Function

The structural design's discrete TO aims to minimize weight while maximizing stiffness and decreasing structural compliance. Thus, applying static loading on each wing component yields static stiffness (for both segments). The mechanical resistance to displacement represents the value of the produced deformation under static load [52]. Based on the displacement, the stiffness can be calculated mathematically as:

$$K(x)u = F \tag{23}$$

where F denotes the vector of nodal forces, and u denotes the nodal displacement. The following equation can then be used to determine the nodal displacement:

$$u(x) = K(x)^{-1}F \tag{24}$$

Constraints on the design response, including limits on stresses and displacements, and other parameters, are indicated in the following equation.

$$\theta\{(x),(u)\}_1 \leq \theta_1^*,\ \theta\{(x),(u)\}_2 \leq \theta_2^*, \ldots \tag{25}$$

To estimate the influence of material density variation on the objective function of maximizing stiffness, the optimization code conducts a sensitivity analysis using the next equation.

$$\frac{dC}{dx_i} = -p(x_i)^{p-1}(x_i)^T(K_i)(u_i) \tag{26}$$

where K_i represents the displacement matrix element and u_i is the displacement vector for ith element.

When performing a sensitivity analysis, elements with a minimum material density are weighted, their characteristics become less significant for the structural design and, therefore, are eliminated in succeeding iterations. When the sensitivity of each element is calculated independently without considering the interconnection between these elements, the discontinuity of materials and volumes may appear, thus resulting in their discontinuity from the main geometry. The optimization iterations continue until the convergence of the objective function and therefore until the iterations meet their convergence criteria.

As stated earlier, the main objective of the structural TO of the morphing wing design is to maximize the wing's stiffness while minimizing its weight. The density-based method is used in conjunction with the static linear method [53], thus resulting in the following mathematical formulation of the TO problem:

$$\begin{gathered} \min f(x) = f(x_1, x_2, \ldots\ldots, x_n) \\ g_j(x) \leq 0, \quad j = 1, \ldots\ldots, m \\ x_{i_{min}} \leq x_i \leq x_{i_{max}} \quad i = 1, \ldots\ldots, n \end{gathered} \tag{27}$$

where the independent variables of the objective function $f(x)$ are the design variables x, the constraints denoted by $g(x)$, and the upper and lower bound constraints x_{min} and x_{max}, respectively.

In the optimization procedure, the design space for each wing component was identified as a separate element. Gradient-based optimization is commonly employed due to its efficiency. The set of constraints was computed using their screening process, which minimized the required gradients. Calculating the gradients of given constraints can be facilitated by distinguishing between active and idle constraints, thus by employing the constraints' screening approach, minimizing the number of responses that include a representative set in an optimization problem. The approximate approach is used in conjunction with the optimization algorithm written and executed in numerical codes.

As a result of the TO, the compliance of static structural stiffness is entirely converted to potential deformation energy [54]. The static stiffness of a structure can be determined using Finite Element Analysis (FEA). The design field's material distribution is optimized by the STO SolidThinking Inspire solver for TO and by the OptiStruct solver for sizing optimization; the latter utilizes algorithms to obtain the shape of the best possible wing components. These two optimizations' strategies determine the best possible solutions for wing components' compliance under set boundary conditions, considering the design constraints to minimize their weights.

5. Materials Selection Strategy and Optimization Methodology

The design and development of a strong, lightweight variable span-morphing tapered wing (MVSTW) require the development of a Multidisciplinary Design Optimization (MDO) strategy so that the designed structure can meet all its constraints. Several optimization methodologies have been performed and combined to create a robust, lightweight wing [31,37].

This research presented here is using previous investigations and evaluates the wing design's performance and weight under design constraints. The key aspect is to balance the wing's strength and lightweight attributes by combining material selection with structural optimization. A literature search was carried out on the materials' parameters with the aim to define the optimal weight-to-strength ratios once their properties were obtained from published experimental results and analyses. The composite materials were selected based on the results of an in-house MATLAB code developed to evaluate their characteristics, such as physical–mechanical properties, availabilities, and costs. Optimization using multiple composite materials is more complicated than when a single material is used, as a high number of variables must be considered throughout the optimization process. The pressure was computed separately for each wing component to ensure more accurate results. The following sub-sections provide details on the settings identified for wing components optimization [55].

5.1. Combination of Material Selection and Size Optimization for Wing Skin Thickness

After the material selection optimization, the wing skin will remain continuous, as sizing optimization will be performed rather than topological optimization. Consequently, long-fiber composites are a viable option for this application. The composite configurations vary in their fibers and matrix material types according to the stacking sequences and direction angles. Among the most crucial factors to consider are the costs of composite materials. For instance, glass fiber can be nearly ten times less expensive than carbon fiber.

The E-Glass composite has been considered in this work, as it is much less expensive than the other fibers and offers comparatively very good properties. The epoxy resin and E-glass properties were employed [56].

Furthermore, the epoxy matrix is isotropic, while the fibers are anisotropic. The fiber/volume fraction was considered to be 60%, and the presence of voids was neglected. The longitudinal properties and Poisson's ratio for the lamina were obtained from the equilibrium, compatibility, and stress–strain relationships, while the transversal Young's modulus was obtained using the Halpin–Tsai method [43]. The next phase is the calculation of the effective composite material mechanical characteristics.

This work will address a composite with eight layers (four symmetrical layers), in a configuration of $[0^\circ/90^\circ/0^\circ/90^\circ]_{syn}$, and the composite laminate can be considered isotropic. The initial thickness of each layer was set to 0.250 mm; therefore, the total thickness of the composite is 2 mm. However, the composite thickness can be adjusted depending on the sizing optimization results. It is feasible to obtain the laminate stiffness matrix and the ultimate properties of laminates by using the extensional stiffness, the coupling stiffness, and the bending stiffness matrices of the laminate [44]. Given that the acquired properties are determined analytically, the yield strength and ultimate strength will be considered as 2.5% of the Young's modulus and 1.5 times the yield strength, respectively. Table 4 below contains a summary of properties obtained using the method described above:

Table 4. Material properties of E-glass composite applied in the Sizing Optimization of the wing skin.

Parameter	Value
Young's modulus (quasi-isotropic)	30.578 GPa
Poisson's ratio	0.138
Yield strength	901.097 MPa
Ultimate strength	1351.645 MPa
Density	2.016 g/cm^3

This investigation used a technique identical to that used priorly [31] for aluminum alloy 2024-T3. For all phases of this study, a baseline wing with an identical skin thickness of 2 mm was employed for its both segments. The outcomes of size optimization (SO) in a 2D field were transferred to those in a 3D field with the aim to develop the best feasible wing skin [57]. It is commonly understood that the Size Optimization (SO) is an iterative process. The CFD and the XFLR5 solvers were used to calculate the aerodynamic loads on a full wingspan extension and at maximum speed to perform the Size Optimization on the wing skin. Meshing was applied to both segments, where the tetra-quadrilateral element size of 20 mm was used on both their lengths, as illustrated in Figure 5.

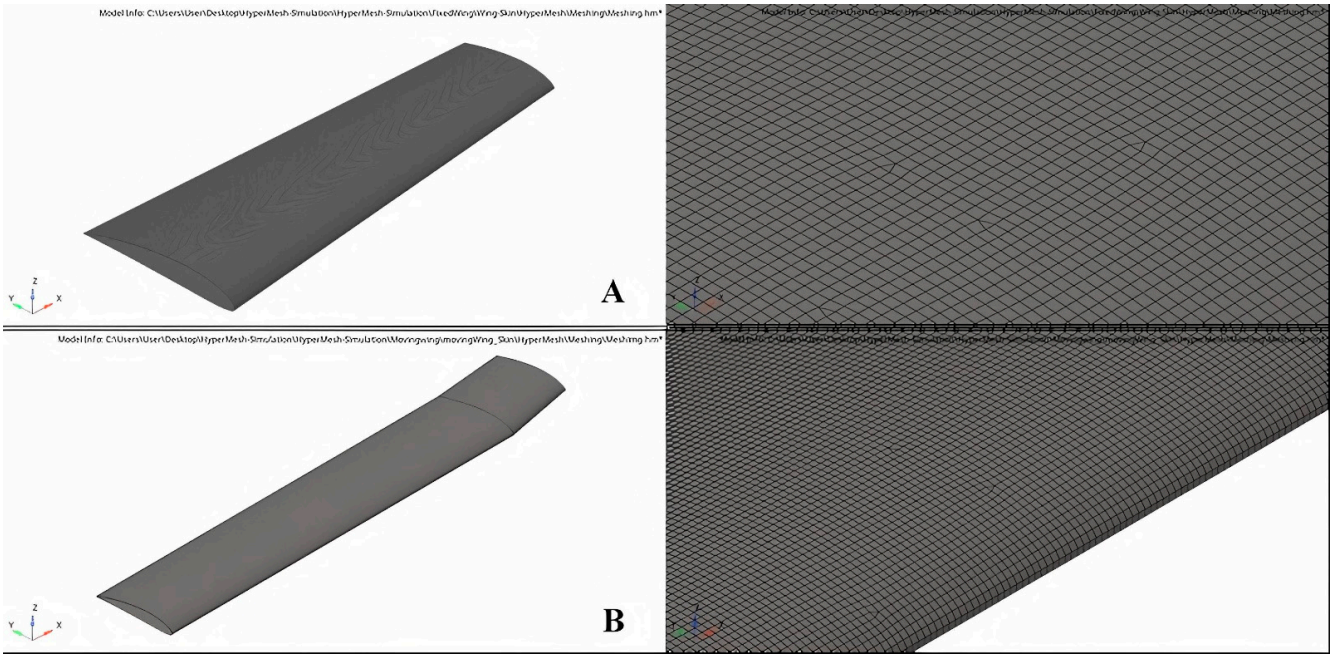

Figure 5. Meshing method for (**A**) fixed wing and (**B**) moving wing.

Aerodynamic loads were used, and their design variables were considered as scalar parameters in the optimization computations. In this investigation, these parameters were determined to solve the optimization problem, as the thickness of the wing skin affects the system's responses. Design volume and set of the stresses were the variables applied to the optimization responses. The objective function was set to decrease the structural components' weights of the wing skin. The lower and upper bounds of the maximum stress values were given as the design constraints. Therefore, the design parameter of the maximum stress response was selected as 750 MPa. The design variable was given an initial value of 2 mm, as well as a lower and upper bound of 0.5 and 2 mm, respectively [58,59]. The following formulation was used to describe the optimization problem:

$$\begin{gathered} \min M \\ \sigma_{max} = 750 \text{ MPa} \\ 0.5 \leq T \leq 2 \end{gathered} \tag{28}$$

5.2. Combined Material Selection and Topology Optimization for Wing Spars

The spars design of the aluminum alloy 2024-T3 based on the Topology Optimization performs effectively, as demonstrated in [31]. The TO aims to maximize the structural stiffness, and then the maximum stress obtained for the optimized component should be less than the yield strength and is used as a reference for selecting alternative lighter materials. Aluminum 2024-T3 has a yield strength of around 345 MPa. The main limitations of this material in terms of its optimization are its geometric shape, i.e., areas that should be preserved intact due to the allocation of structures inherent to the mechanism or for the load distribution continuity.

Long-fiber composite materials, widely utilized in the aerospace industry, would be very good candidates for this application. However, the spars should be topologically optimized, and so there would be several regions with cut-outs, according to an earlier investigation in which aluminum alloy 2024-T3 was used for the wing spars' design [31].

Avoiding the fibers' cut-out requires a more expensive manufacturing technique, and the material properties of such spars after machining will be less predictable. Therefore, composite materials with long fibers would be inappropriate for this application. Polymers, however, have a low manufacturing cost, moderate to high strength, and low-density properties [60]. High-Density Polyethylene (HDPE) has been tested to evaluate its properties for use in structural applications [60,61]. HDPE could be derived from virgin manufacturing or from 100% recycled HDPE. While the environmental benefit of recycled HDPE is significant, the percentage of impurities in the material could be a limitation, as HDPE is commonly used in conjunction with other polymers, such as polypropylene (PP) [62].

Numerous papers detail the mechanical characteristics of pure HDPE. The values acquired from various sources are averaged for this work [60–63]. In terms of Poisson's coefficient, the value of 0.4 is considered as shown in Table 5, the same as the value used by Contino et al. in [64].

Table 5. Material properties of HDPE applied in the topology optimization of the wing spars.

Parameter	Value
Young's modulus	1250 MPa
Poisson's ratio	0.4
Yield strength	28 MPa
Ultimate strength	48 MPa
Density	0.95 g/cm^3

In aircraft wings, the spar is one of the most critical components, as it must be able to withstand the most severe aerodynamic loads and to provide support for other wing components. A spar is an extended beam that is installed on the length of the wingspan and provides support to the wing when subjected to bending loads. In other words, it should be strong enough to support the effects of tensile, compressive, and shear loads. The afore-mentioned TO for baseline solid wing design has been proposed, using two spars at predetermined locations for each wing segment, as seen in Figure 6 [37].

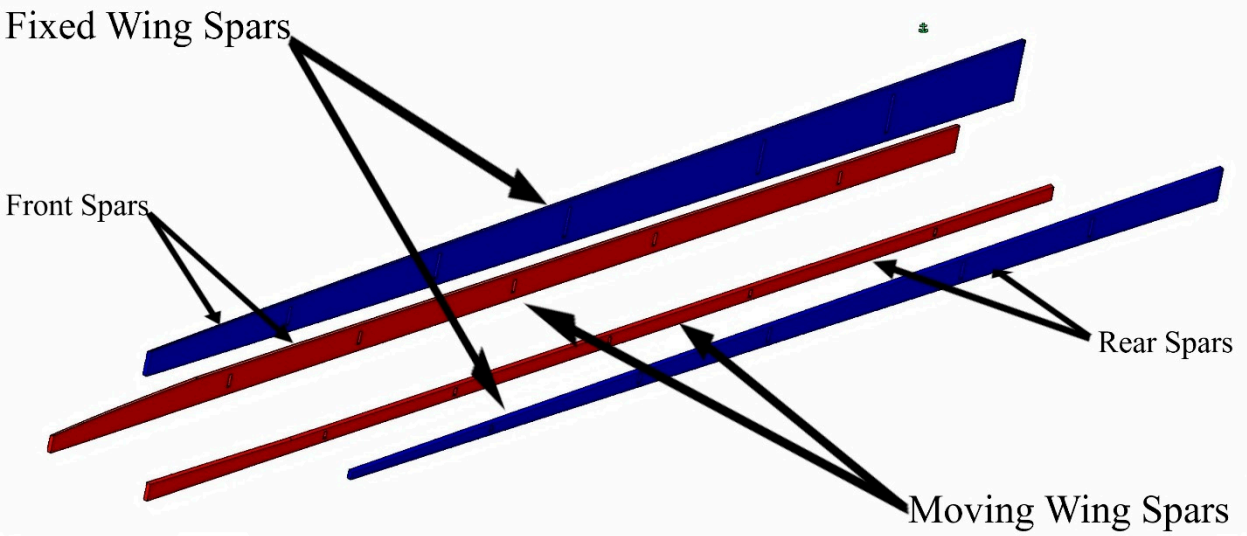

Figure 6. Baseline geometrical shape for morphing wing spars at their initial position for fixed and moving segments.

The aerodynamic loads were calculated using the ANSYS Fluent and XFLR5 software tools, with the spars modeled as beams with discrete loads at various locations (Table 3 gives their values). The structural weights of wing spars were considered when formulating the problem for the wing spars, as the primary objective was to determine the ideal structural parameters of the wing. This objective made it possible to establish the wing's minimal weight while still meeting the constraints of strength, durability, and versatility [36].

The same approaches as those considered in the previous optimization were used to determine the I-beam sections. The fundamental motivation for using an I-beam section (except where it links to the ribs) is its significant mechanical advantages over other beam configurations. The I-beam shape supports the other wing components extremely well, resists mechanical strain (such as torsion and deformation), decreases the load intensity on the other components, and lowers weight and costs [65,66].

All wing spars underwent identical analysis techniques in a 3D environment [67].

Figures 7 and 8 show the specified designable and non-designable portions of the front and rear spars with their associated boundary conditions for fixed and moving wing segments, respectively.

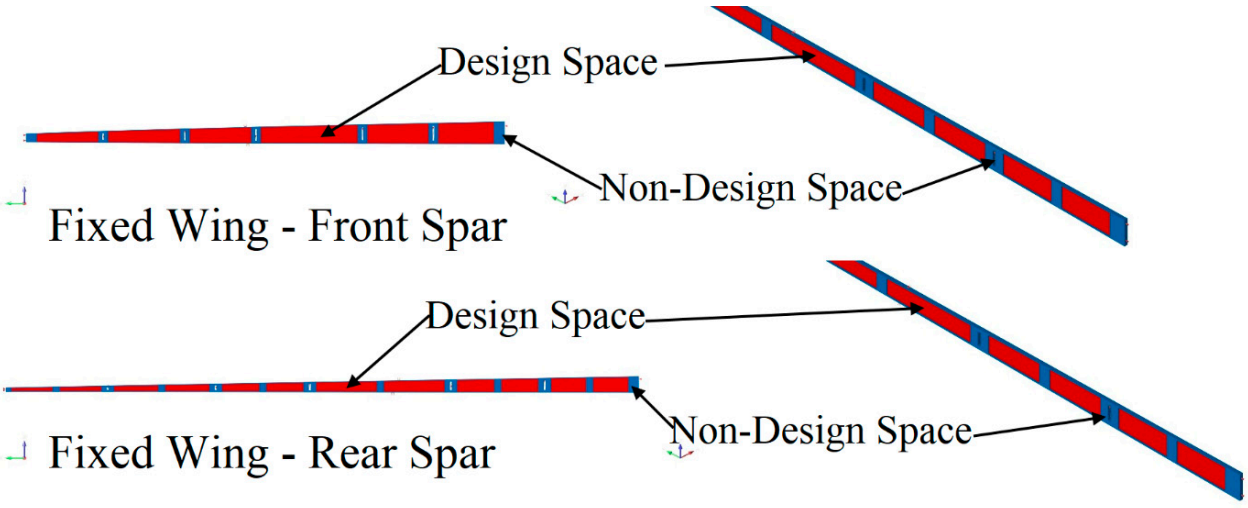

Figure 7. Boundary conditions with design and non-design spaces for the front and rear spars of a fixed wing.

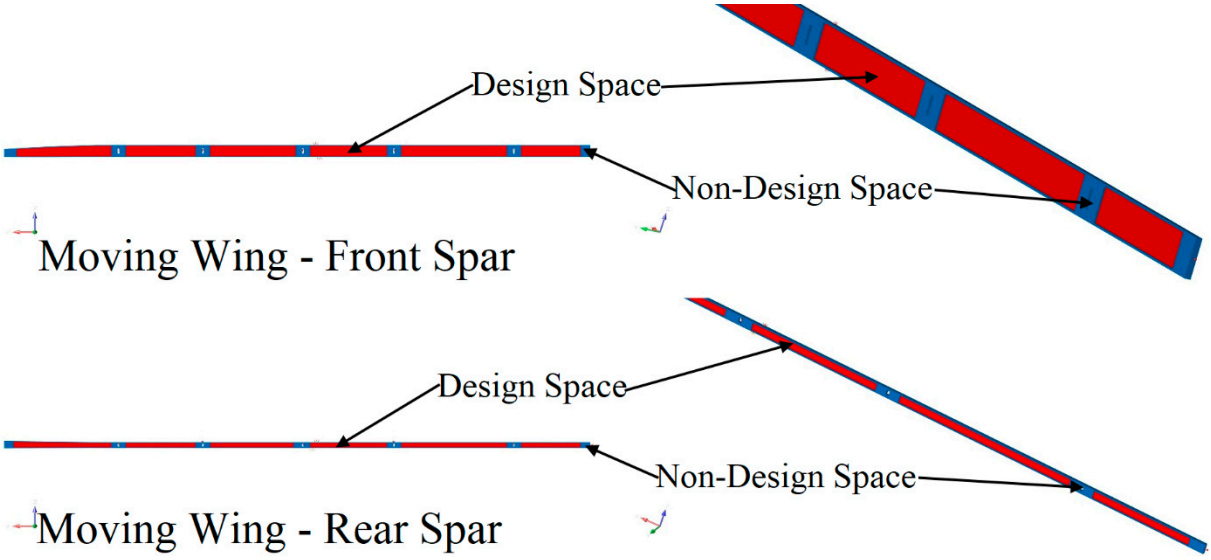

Figure 8. Boundary conditions with design and non-design spaces for the front and rear spars of a moving wing.

5.3. Combined Material Selection and Topology Optimization for Wing Ribs

As in the case of spars, the priority for an initial analysis of unconventional materials for wing ribs was focused on polymers. Since the rib geometry is critical to the wing aerodynamics, its manufacturing should be precise and repeatable. Therefore, 3D printers were utilized to reduce costs, speed up production, and increase accessibility.

When considering three-dimensional printing, various factors in addition to the printing material affect the final product's mechanical qualities, such as the manufacturing method. Acrylonitrile Butadiene Styrene (ABS) is one of the first polymers that was widely used in 3D printers, and its properties are well known in the extensive documentation. Nomani et al. [68] Describe the thickness effects of each ABS layer on the final product's tensile and compression properties, revealing that, in general, increasing the thickness of each layer results in a decrease in the Young's modulus, ranging from 2.0 GPa for a thickness of 0.2 mm to 1.55 GPa for a thickness of 0.8 mm.

The ABS Poisson's ratio was investigated by Cantrell J. et al. [69]. According to their research findings, Poisson's coefficient exhibits little variation in relation to print/raster orientation. The values obtained ranged from 0.36 to 0.38.

Thus, Poisson's coefficient of 0.36 will be used for the ABS in this work. Table 6 below highlights the ABS properties that have been considered in the investigations mentioned above [55,56].

Table 6. Material properties of ABS applied in the topology optimization of the wing ribs.

Parameter	Value
Young's modulus	2000 MPa
Poisson's ratio	0.36
Yield strength	30 MPa
Ultimate strength	36 MPa
Density	1.05 g/cm^3

As illustrated in Figure 9, the wing baseline of the previous TO offers a total of seven ribs for each wing segment, with estimated lengths between the ribs on the wings [37]. These ribs are intended to minimize wing deformation by keeping the geometrical structure of the wing's sections. Therefore, the wing's outward loads are distributed equally across the skin and wing components. As shown in Figure 9, a cavity should be included in

the fixed wing ribs to accommodate the moving wing. The TO was therefore applied to the interior six ribs of each wing segment. The exterior ribs for each wing segment were excluded from design optimization as the last rib of the fixed wing should be solid and only hold the cavity of the moving wing. Furthermore, the ribs of the moving wing should have a solid shape for better aerodynamic efficiency.

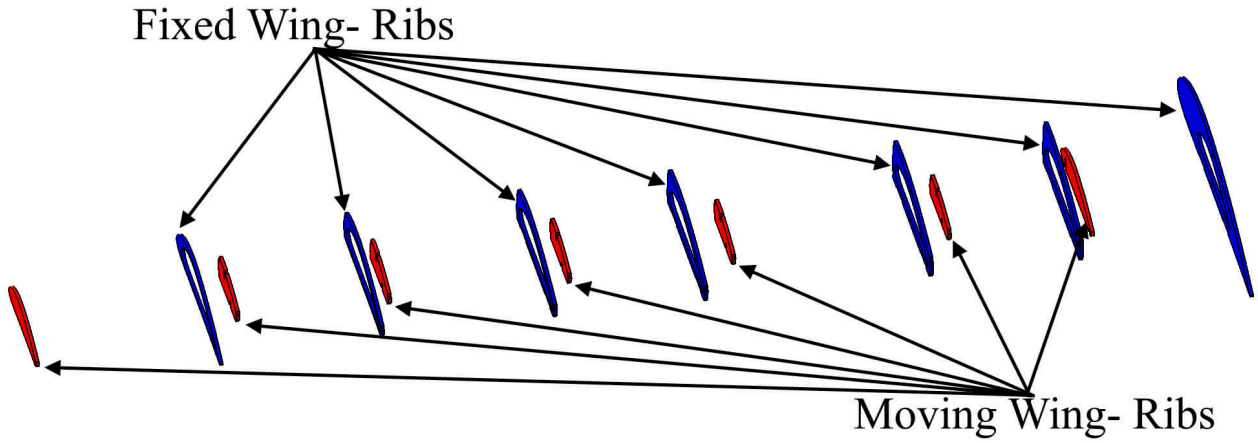

Figure 9. The geometric shape of morphing wing ribs for fixed and moving wings.

The original design space layout and boundary conditions were applied to establish the optimal material distribution inside the ribs. Ribs for each wing were discretized into separate components, and node numbers were assigned to them according to their sizes on both wings. Figures 10 and 11 illustrate the boundary conditions of ribs of both wing segments.

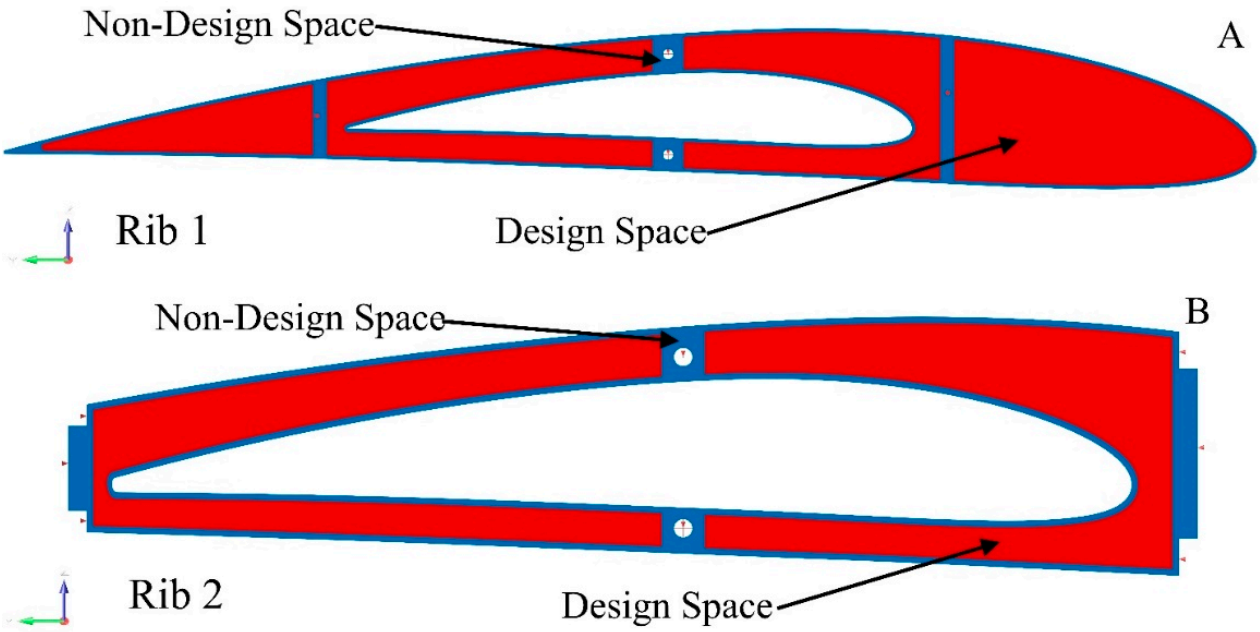

Figure 10. Examples of the boundary conditions, designable space, and non-designable space for ribs 1 and 2 of the fixed wing.

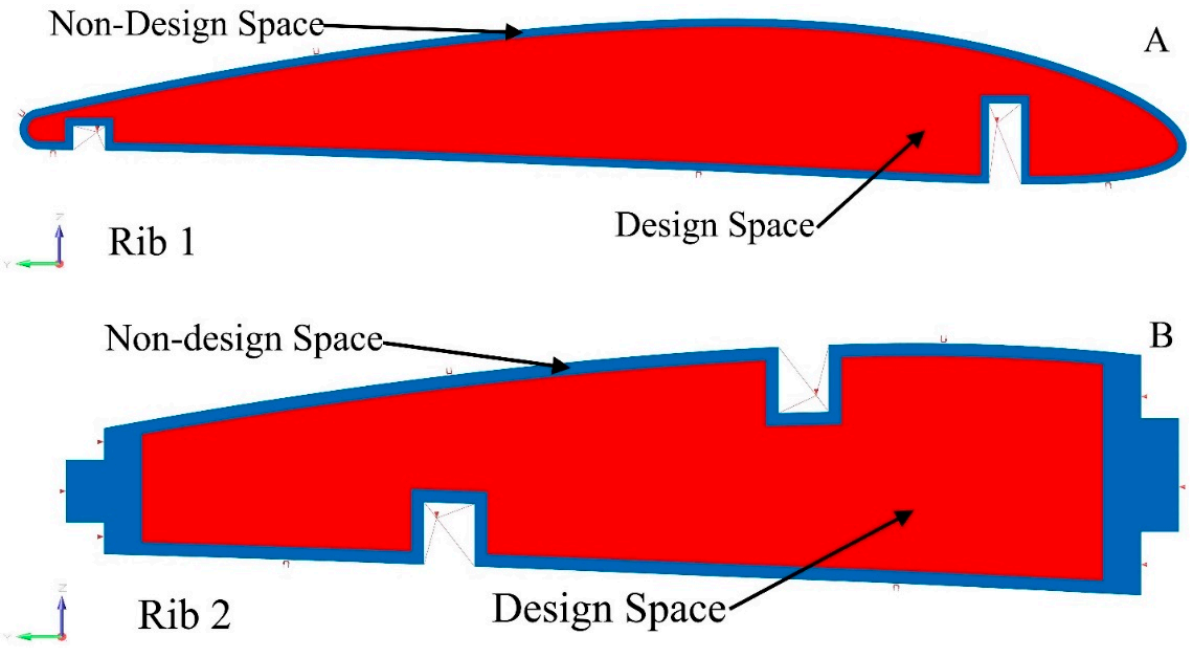

Figure 11. Examples of the boundary conditions, designable space, and non-designable space of ribs 1 and 2 of the moving wing as an example.

By considering the wing ribs as an opposing constraint, a volume constraint was applied to all of them in the optimization problem. The loads acting on each rib can be computed efficiently by aerodynamic optimization, as indicated in Table 4. The designable areas and the rib edges were also included in the objective function. Connection locations linking the ribs within the spars were not included in the TO process; they were considered non-designable regions. Areas that were not designable at sparse connection locations were fixed during optimization because they were not included in the design field.

5.4. Combined Material Selection and Topology Optimization for Wing Support Element's Structure

The wing's support elements are crucial to a wing structure's integrity, and thus to the design of a robust wing. Several composite materials were investigated to determine the most appropriate materials for this project. The material selection criteria were subjected to various parameters, including cost, mechanical behavior, and availability on the market. Three materials were adopted for support elements: balsa wood, white oak, and aluminum alloy 6063-T6.

The excellent lightweight and insulating characteristics of balsa wood have made it a commercially important material in many applications, where it was used as the core of sandwich-type constructions for critical weight applications in aircraft and ship structures. Its radial mechanical characteristics are affected by the bending of the fibers, as well as by the axial compression of the rays under radial stresses [70,71].

Table 7 shows the material properties of balsa wood.

Table 7. Material properties of balsa wood applied in the topology optimization of the wing support elements.

Parameter	Value
Young's modulus	3.4 GPa
Poisson's ratio	0.23
Yield strength	21.6 MPa
Ultimate strength	21.6 MPa
Density	0.16 g/cm^3

White oak is used in various industrial applications due to its desirable qualities. White oak (Quercus alba), a relatively high-density ring-porous hardwood, was used to build several support elements for our wing [72].

Table 8 shows its material properties.

Table 8. Material properties of white oak applied in the topology optimization of the wing support elements.

Parameter	Value
Young's modulus	12.27 MPa
Poisson's ratio	0.369
Yield strength	104.8 MPa
Ultimate strength	104.8 MPa
Density	0.68 g/cm^3

The aluminum alloy 6063-T6 was used to design other support elements. Isotropic aluminum alloy 6063-T6 offers very good durability and high solidity and fatigue resistance. [73]. Table 9 shows its material properties.

Table 9. Material properties of aluminum alloy 6063-T6 applied in the topology optimization of the wing support elements.

Parameter	Value
Young's modulus	68.9 GPa
Poisson's ratio	0.33
Yield strength	214 MPa
Ultimate strength	241 MPa
Density	2.7 g/cm^3

The leading-edge ribs, trailing-edge ribs, stringers, and stiffeners for the optimized wing based on the TO approach were developed using an initial design for the baseline wing. Each wing segment's support elements were built as shear webs to provide stability and to withstand buckling, bending, torsion, and vertical shear loading. Along with aerodynamic and inertial loads acting on the wings, various loads depending on their shapes and structural masses might be considered during the design process. Furthermore, the payload, which can be on electronic equipment or a monitoring camera, may be carried on the wings or in the fuselage. This equipment adds weight as increases to the wing's bending, shear, and torsion loads.

Wing components with shear web structures offer a reliable design by distributing loads on the wing in multiple directions. The structure and materials of the support elements for both segments of a VSMTW are illustrated in Figure 12.

The boundary conditions applied to the support wing elements matched the boundary conditions for the spars and ribs. The structure of the wing's support elements and their boundary conditions were calculated using parametric data from the aerodynamic optimization, as shown in Table 3. Since the weight of the support elements greatly contributes to the overall weight of the wing, its minimization while preserving its stiffness is crucial.

The boundary conditions that apply to the support elements vary according to the component's dimensions. Figures 13 and 14 depict the boundary conditions of several support components for the fixed and moving wing, respectively. The volume constraint was applied to the support element structure, which functioned as an opposing constraint in the optimization process.

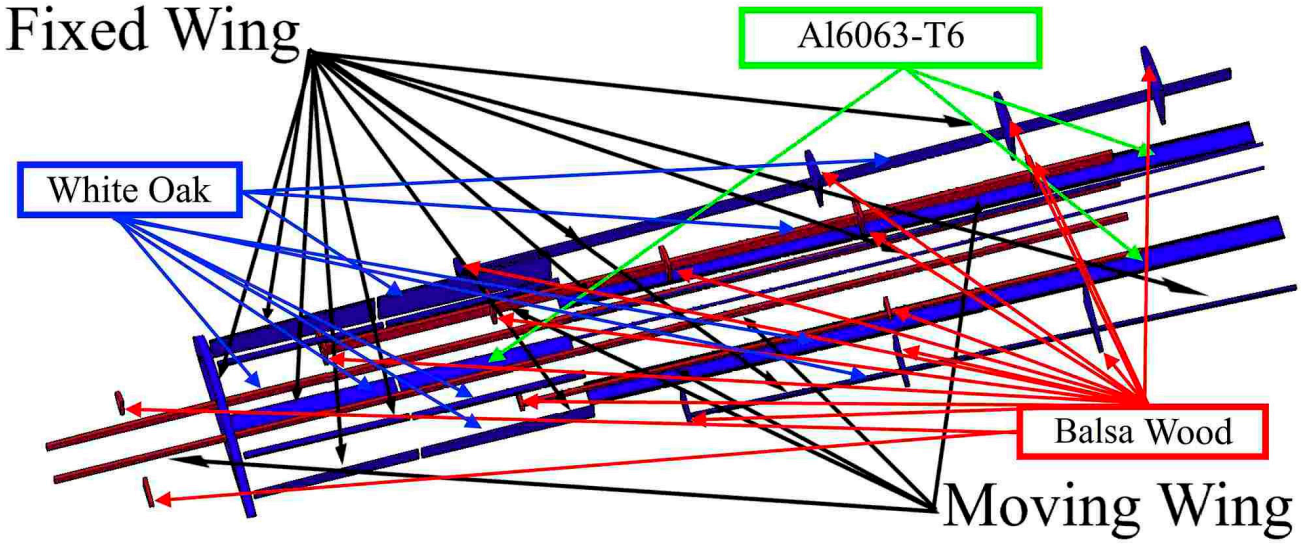

Figure 12. Support elements with their materials for each wing component for fixed and moving wings at their original positions.

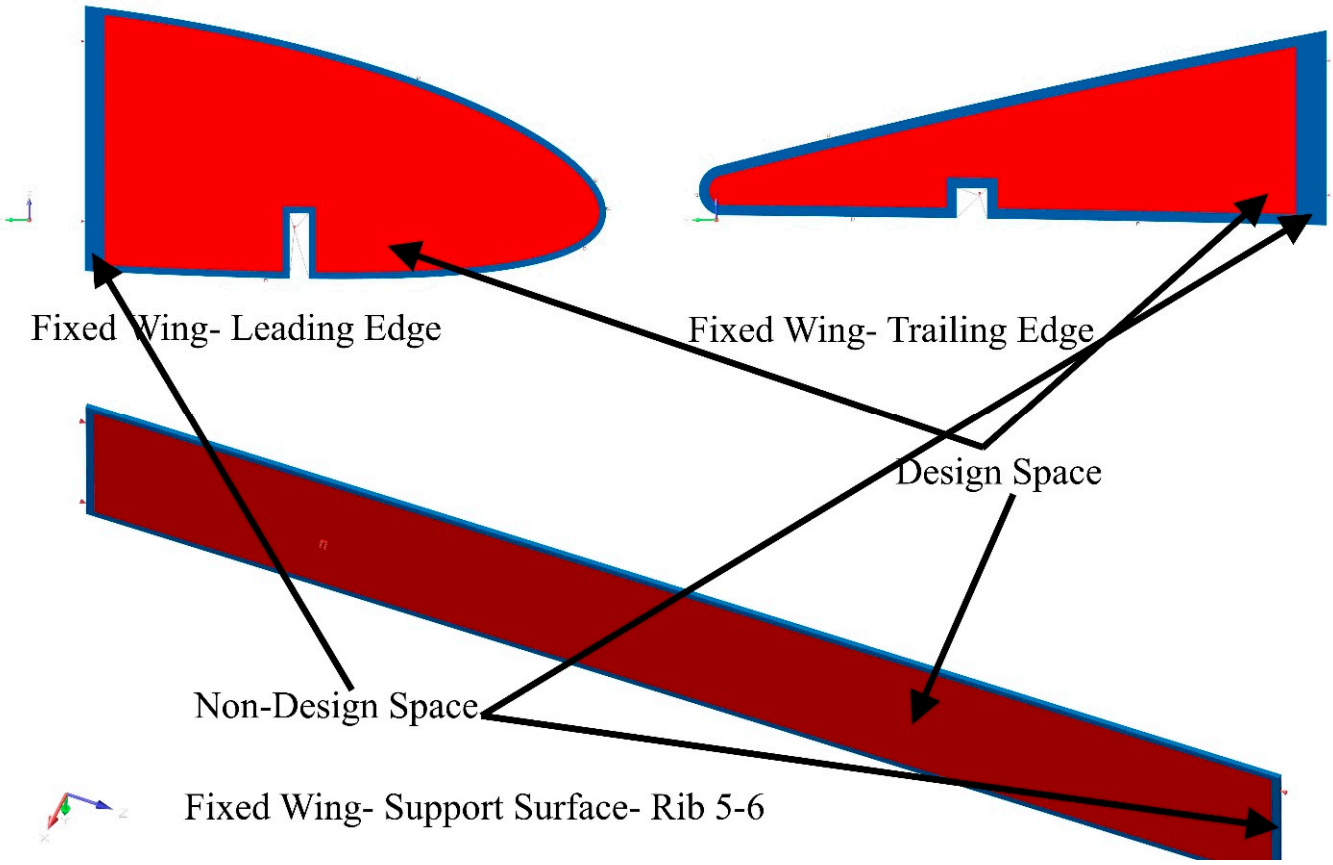

Figure 13. Boundary conditions, designable space, and non-designable space as examples for support elements (leading-edge rib 1, trailing-edge rib 1, and bottom support plate between ribs 5 and 6) for a fixed wing.

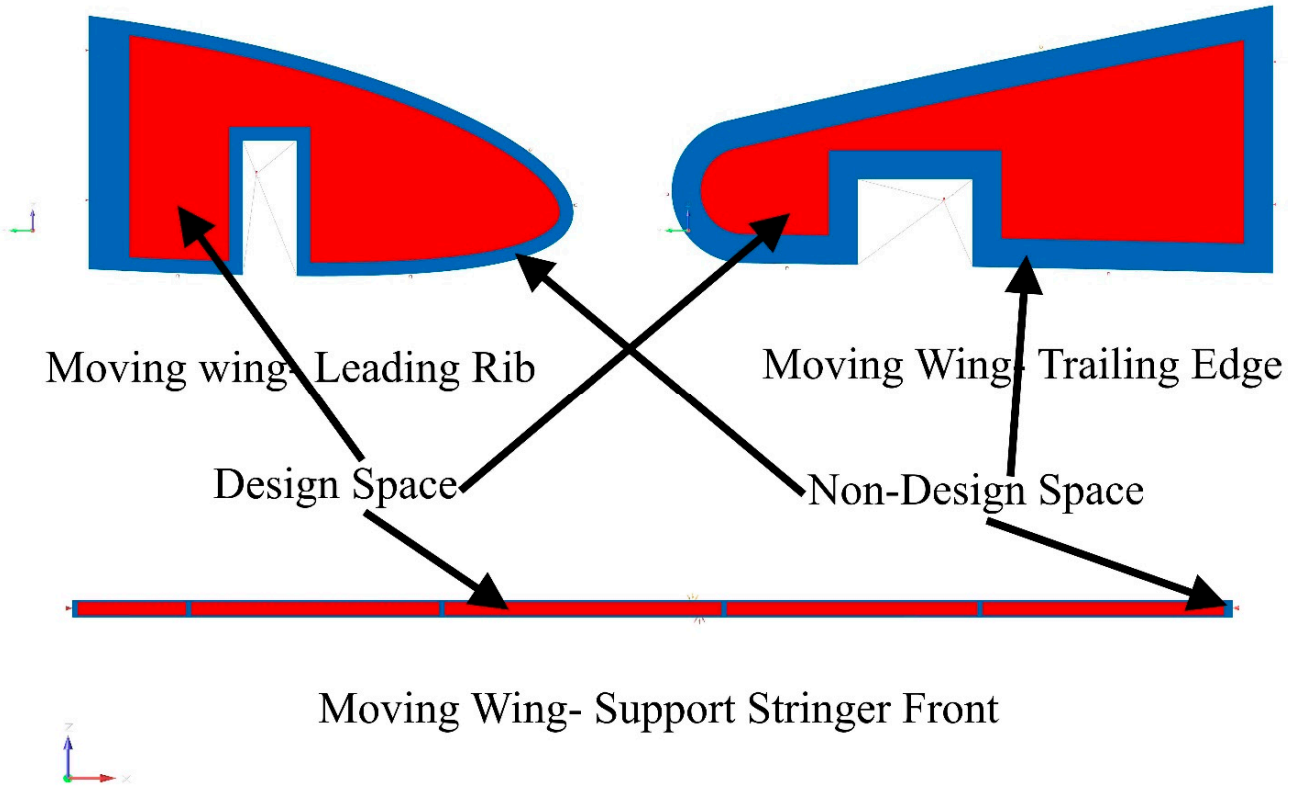

Figure 14. Boundary conditions, designable space, and non-designable space as examples for support elements (leading-edge rib, trailing-edge rib, and support stringer front) for a moving wing.

The area between the wing components attached to others cannot be altered from its original design, as it links each component to the others. The edges of the support elements and the sites where the support element components are bound to other wing components were thus determined to be non-designable. Due to the multiple locations where connections between wing components must be established, these components were specified with their fixed regions throughout the TO. They indicate the connections with other wing components and can thus be modified throughout the optimization process.

6. Multidisciplinary Optimization Results and Evaluation

Aerodynamic analysis, material selection code, and structural optimization STO were performed on the VSMTW, as described in the preceding sections, to improve the UAS-S4′s capabilities under various flight scenarios. Altair's Inspire and OptiStruct tools provide design engineers with the most powerful and user-friendly generative design/optimization and quick simulation solutions. The optimization problem was then solved with multi-disciplinary numerical optimizations. This optimization problem takes into account the parameters that define the overall performance.

These parameters were treated as either optimization objectives or constraints during the optimization process. Size and topology variables were used to determine the thickness of the skin and the optimized structure of the other wing components, respectively. The same design constraints were imposed on the structural stiffness to conduct the wing skin's size optimization (SO) for both segments. Figure 15 shows how a few optimization iterations were applied to rapidly converge to the optimal solution with a highly efficient skin thickness.

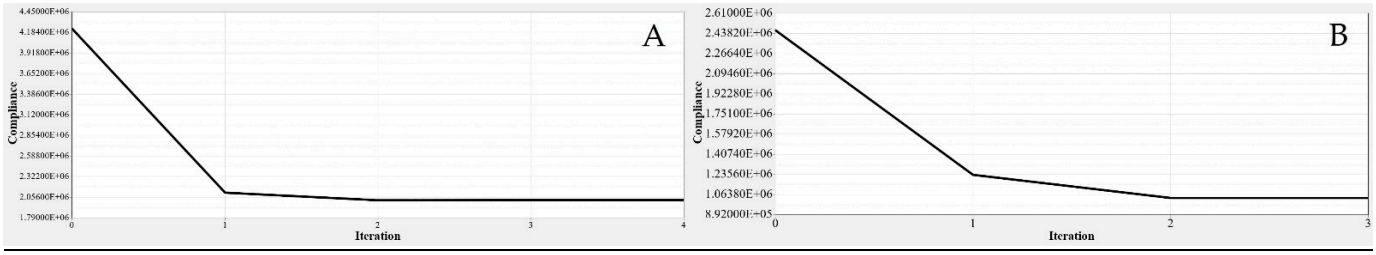

Figure 15. The objective function convergence graphs for (**A**) fixed wing skin and (**B**) moving wing skin.

The SO was carried out on each wing segment. Figure 16 illustrates the results of the study's interpretations for both types of wing segments.

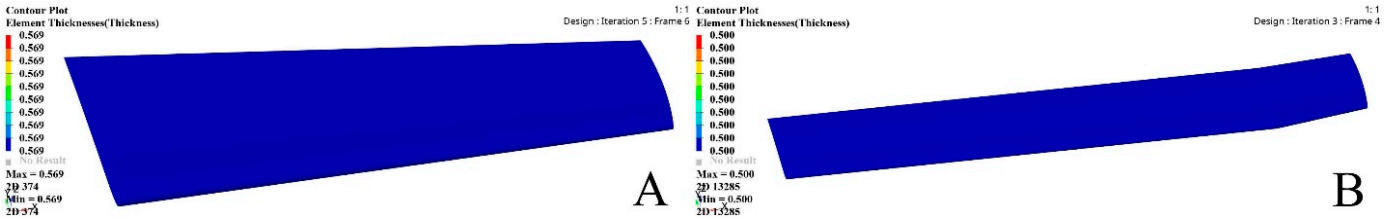

Figure 16. The thickness obtained based on sizing optimization (SO) results for (**A**) fixed wing and (**B**) moving wing.

To serve as a reference for size optimization, the base wing for fixed and moving segments was designed with a thickness of 2 mm. Figure 17 illustrates the FEM results for estimating the optimized wing thickness for both wing skins. This optimization is based on a FEM static analysis performed under extreme flight conditions, during which stress and deformation were generated.

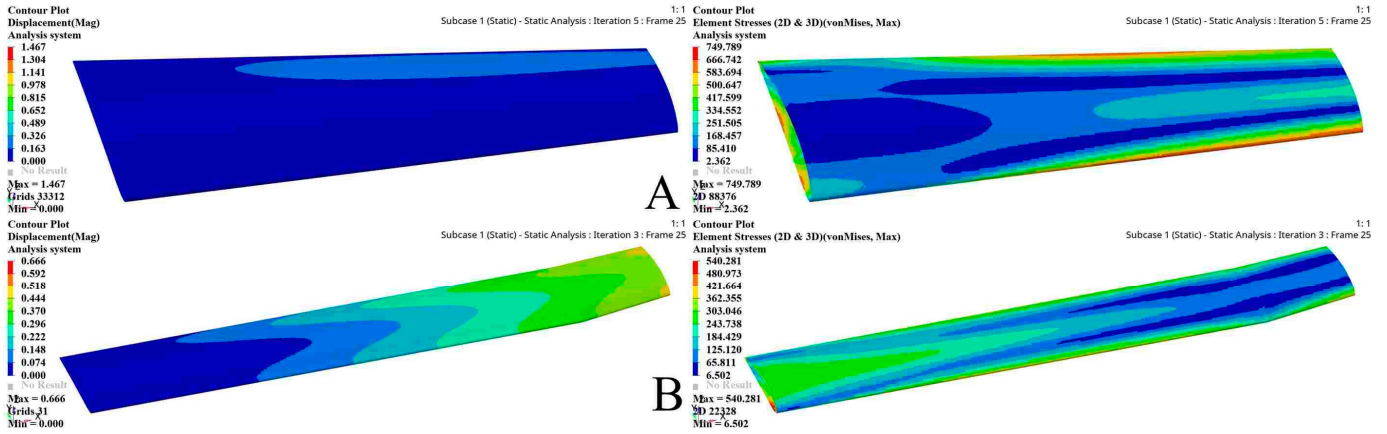

Figure 17. The sizing optimization problem FEM results for fixed (**A**) and moving (**B**) wing segments.

The maximum stress value used in the Size Optimization (SO) of the wing applied to both segments' skins was limited to 750 MPa in order to obtain the optimal thickness capable of achieving the highest efficiency to withstand the aerodynamic loading. Both wing segments were subjected to identical boundary conditions, and SO and FEM analyses were conducted according to the wing volume and shape. The maximum deformations and stresses obtained under extreme flight scenarios, as well as other key parameter values resulting from the optimization results, are summarized in Table 10.

Table 10. Evaluations obtained via SO and FEM for the wing skins for both wing segments.

	Iterations	Deformation	Stress	Original Skin Thickness	Optimized Skin Thickness	Weight Reduction Ratio
Fixed Wing	5	1.47 mm	749.79 MPa	2 mm	0.569 mm	81.45%
Moving Wing	3	0.67 mm	540.29 MPa	2 mm	0.500 mm	81.80%

To apply the TO, multidisciplinary numerical optimization was used to define the optimized spars that would provide maximum wing stiffness while reducing the wing weight. The aerodynamic investigation determined the maximum aerodynamic pressures for extreme flight scenarios. The wing structure was investigated aerodynamically at sea level and at maximum speed (68 m/s) with the aim to achieve the appropriate distribution of aerodynamic loading across the wingspan, as depicted in Table 11. Altair's SolidThinking Inspire software was used to fulfill the TO objective. The initial wing spars' topology and shape were optimized to minimize the structural compliance and to maximize the structural stiffness to weight ratio while remaining within the target envelope's restrictions.

Table 11. The parameters of the wing segments for spars were determined by TO using Finite Element Analysis (FEA).

	Fixed Wing		Moving Wing	
	Front Spar	Rear Spar	Front Spar	Rear Spar
Initial Weight	0.29 kg	0.16 kg	0.19 kg	0.59 kg
Optimized Weight	0.17 kg	0.11 kg	0.12 kg	0.08 kg
Weight reduction Ratio	41.4%	31.3%	36.8%	86.4%
Displacement	0.00015 mm	0.00056 mm	0.00020 mm	0.00057 mm
Stress	0.2016 MPa	0.3191 MPa	0.1869 MPa	0.1973 MPa
Safety Factor	31,830	66,130	2,864,000	4,264,000

The volume fraction of 30% was used to obtain the maximum structural stiffness and then to use that value as an optimization constraint. The design variable is the structural weight associated with an assigned global compliance-based stress. The TO results are summarized in Table 11.

Figure 18 depicts an iterative process for determining the element density based on the TO results of the wing spar and as shown in Table 10. Table 11 shows the parameters of the most critical wing spars as a function of the design parameters. The advantage of using TO in SolidThinking Inspire is that the FE characteristics are changed according to the optimization results. The FE characteristics obtained using the TO are shown in Figures 19–21. Table 11 lists the weights of the original and optimized spars, thus revealing a considerable reduction in the average weight.

This component-analysis-based TO methodology leads to a comprehensive structural design and offers an alternate method for minimizing the structural weight of wing spars. The results shown in Table 10 also demonstrate that the component-analysis-based TO strategy for high effectiveness and reliability in the continuum design of wing components can be a practical and logical design technique.

The wing ribs were subjected to similar steps as those applied to the wing spars calculations. According to its computed aerodynamic loading, an optimization approach based on the Finite Element Model (FEM) was constructed for each rib. Design variables were determined, including the material density of each element. Two analysis responses were identified, which were described in terms of structural compliance and volume fraction, with the volume fraction classified as a constraint and the compliance characterized as an objective function. The volume fraction was used as a constraint in the standard TO configuration, which resulted in compliance minimization. Figure 22 illustrates the distribution of material density of the wing ribs as determined by TO. The FE models

developed for the specified ribs based on the TO approach illustrated in Figures 23–25 reveal that significant weight savings were achieved without compromising component stiffness.

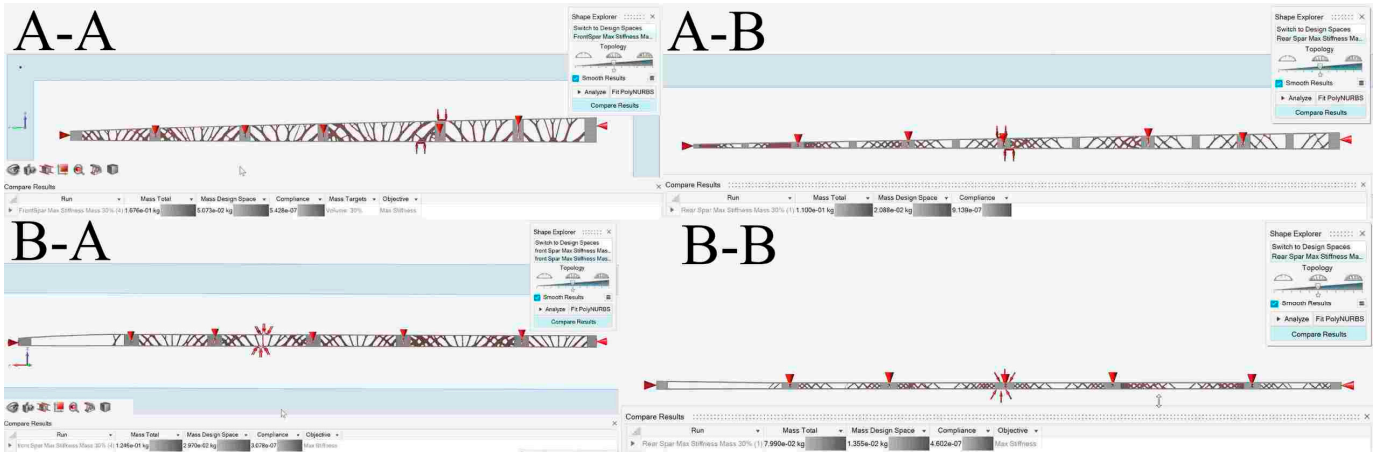

Figure 18. Variation in element density obtained using the TO for (**A-A**) fixed wing front spar, (**A-B**) fixed wing rear spar, (**B-A**) moving wing front spar, and (**B-B**) moving wing rear spar.

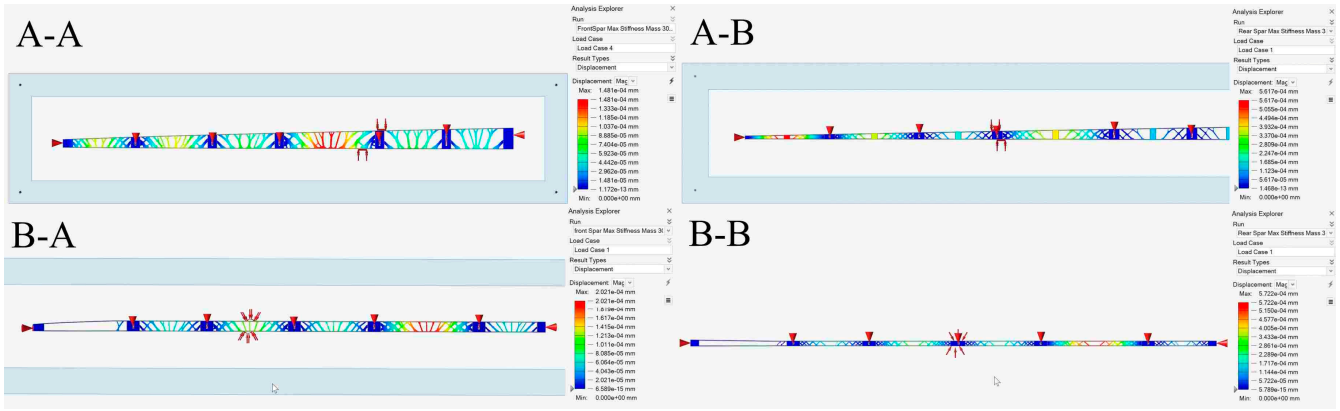

Figure 19. Displacement values obtained using the TO for (**A-A**) fixed wing front spar, (**A-B**) fixed wing rear spar, (**B-A**) moving wing front spar, and (**B-B**) moving wing rear spar.

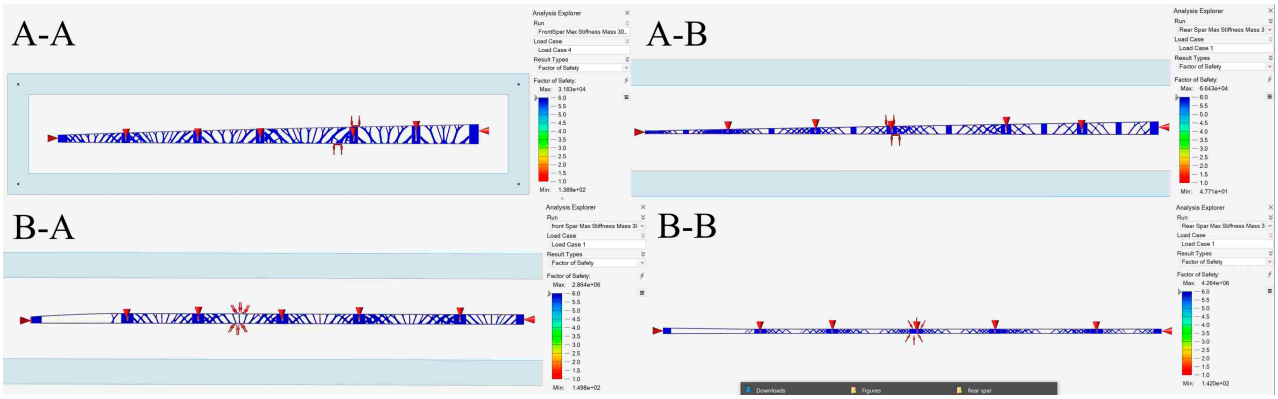

Figure 20. Safety factor evaluations obtained using the TO for (**A-A**) fixed wing front spar, (**A-B**) fixed wing rear spar, (**B-A**) moving wing front spar, and (**B-B**) moving wing rear spar.

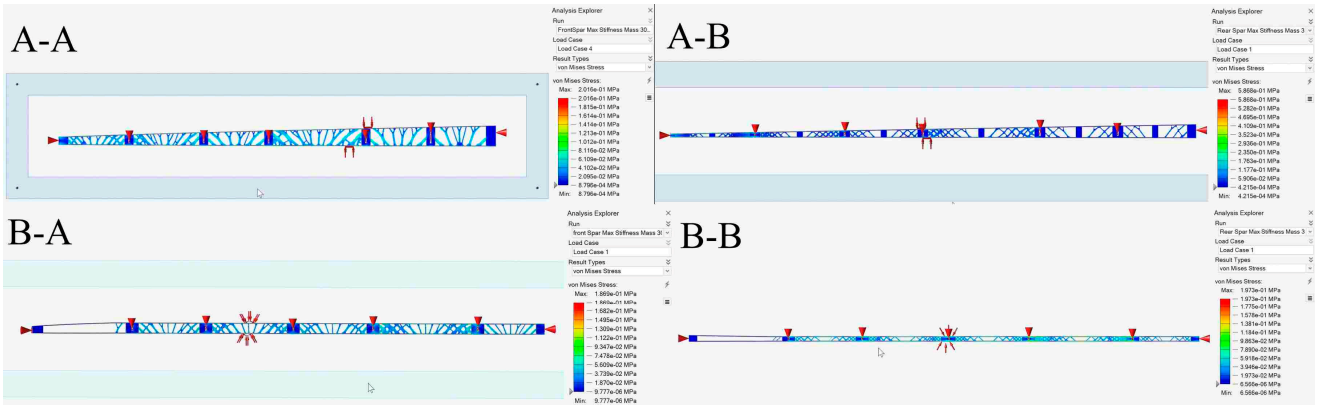

Figure 21. Von mises stress values obtained using the TO for (**A-A**) fixed wing front spar, (**A-B**) fixed wing rear spar, (**B-A**) moving wing front spar, and (**B-B**) moving wing rear spar.

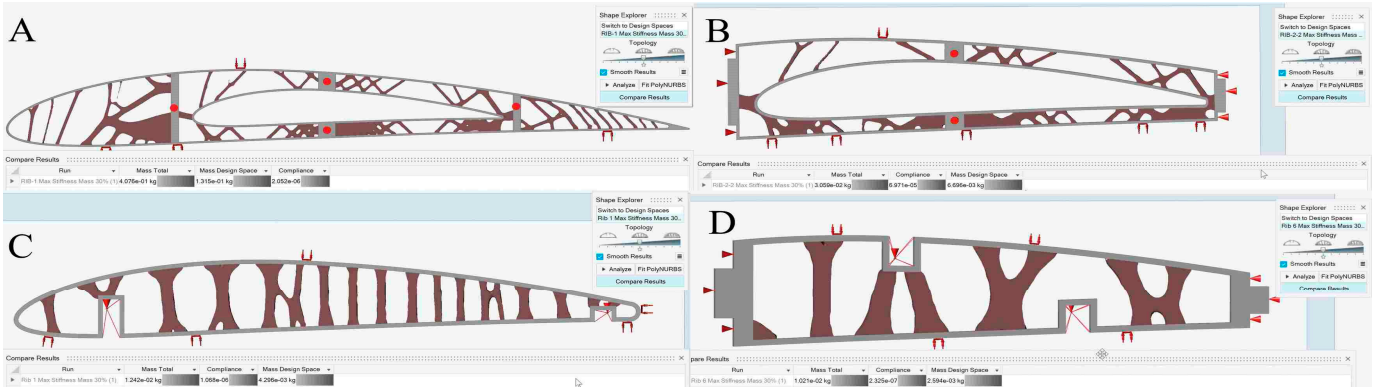

Figure 22. Variation in element density obtained using TO for (**A**) fixed wing rib 1, (**B**) fixed wing rib 2, (**C**) moving wing rib 1, and (**D**) moving wing rib 6.

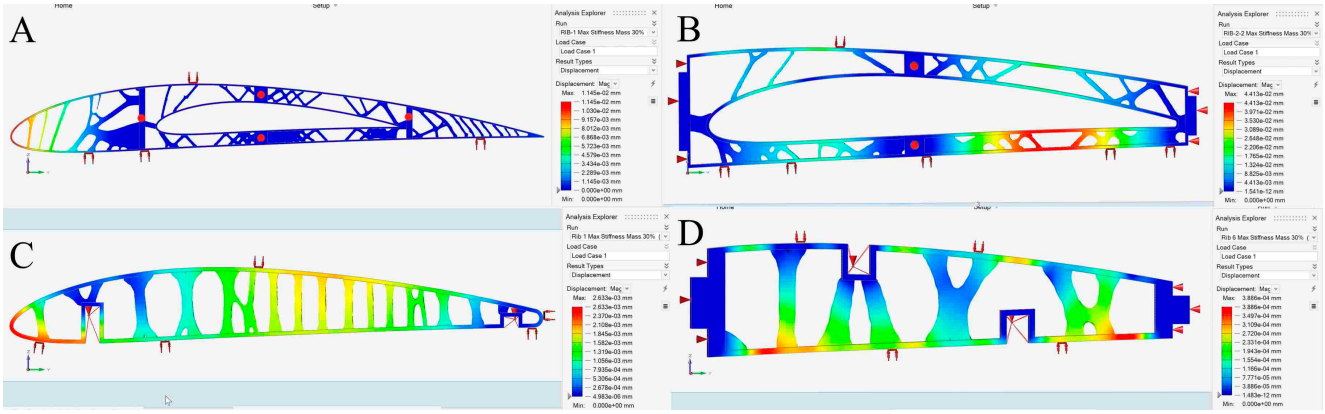

Figure 23. Displacement values obtained using TO for (**A**) fixed wing rib 1, (**B**) fixed wing rib 2, (**C**) moving wing rib 1, and (**D**) moving wing rib 6.

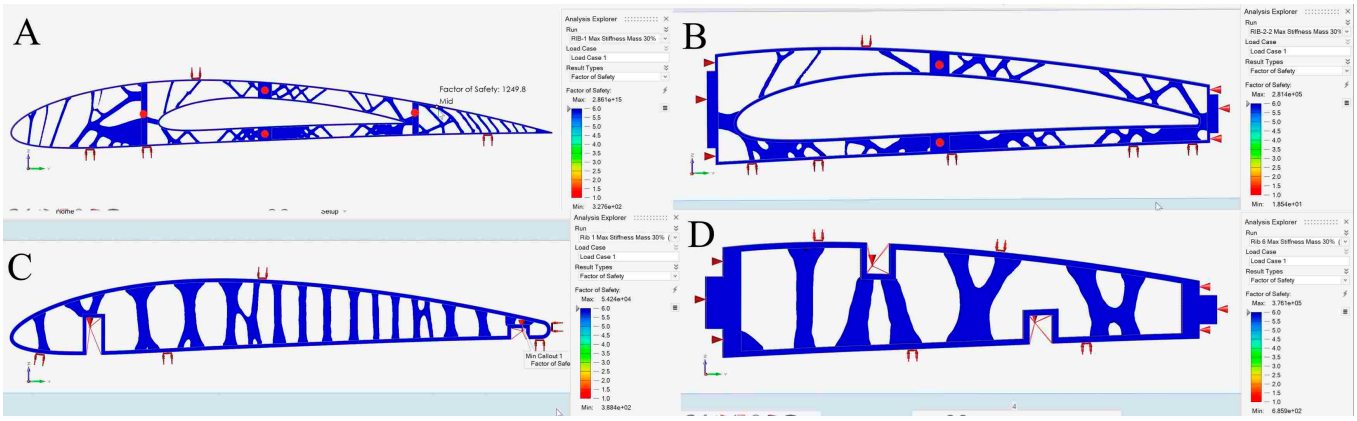

Figure 24. Safety factor evaluations obtained using TO for (**A**) fixed wing rib 1, (**B**) fixed wing rib 2, (**C**) moving wing rib 1, and (**D**) moving wing rib 6.

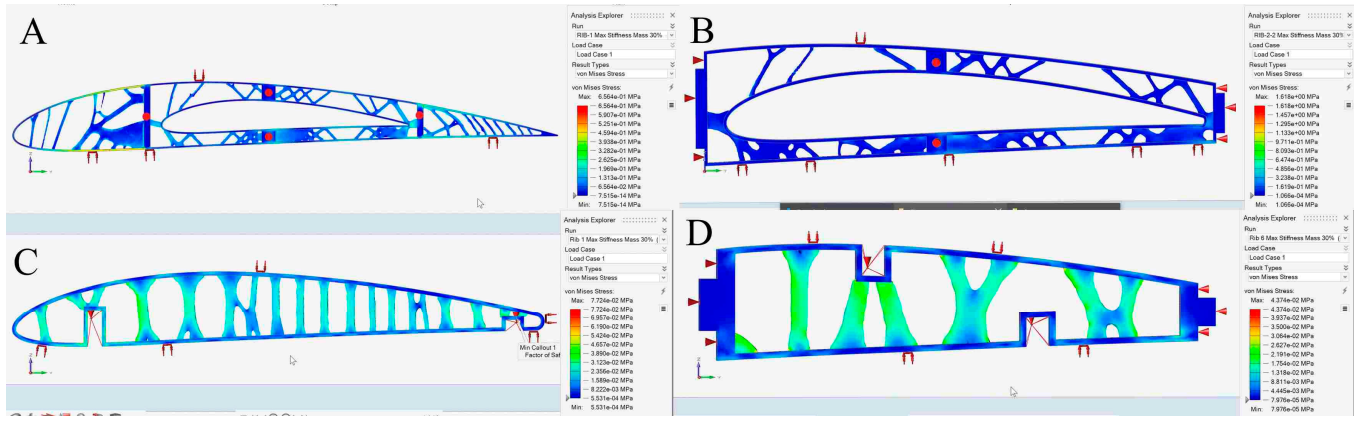

Figure 25. Von mises stress values obtained using TO for (**A**) fixed wing rib 1, (**B**) fixed wing rib 2, (**C**) moving wing rib 1, and (**D**) moving wing rib 6.

The outcomes of the MVSTW rib obtained by TO are shown in Table 12 for their different initial values determined via the distribution of aerodynamic loads. When the ribs' weights before and after optimization were compared, their weights were minimized due to the calculated loads on them. All ribs had extremely low maximum loads and displacements; hence, the optimized ribs met the required strength and stiffness. The wing components, including spars, ribs, and support elements, are shown entirely in blue color, and are not at risk of mechanical failure under corresponding load cases, as indicated in Figures 20, 24, 29 and 32. Thus, the optimized variable span-morphing wing can withstand the extreme aero-mechanical loads encountered throughout varied aircraft missions. Given that these wings should be solid, the seventh rib for both the fixed and moving wing segments was eliminated from the optimization procedure.

The optimized wing segments represented as solids imply that a wing should incorporate TO support elements to meet its design requirements. Table 3, as well as Figures 3 and 4 show the different aerodynamic load situations used to design the support elements for extreme flight conditions. The TO was performed on the structure of the support elements for both wing segments under the specified load cases. The support elements' density cloud maps were represented using the results of several TOs, as illustrated in Figures 26 and 27 for fixed wing and moving wing, respectively. Figures 28–30 show how a TO method affects structural changes in mechanical parameters for fixed segments, such as deformations and stresses.

Table 12. Topology optimization according to Finite Element Analysis yielded these wing segment parameters for the ribs.

		Initial Weight	Optimized Weight	Weight Reduction Ratio	Deformation	Min Factor of Safety	Stress
Fixed Wing	Rib 1	0.094 kg	0.054 kg	42.6%	1.02 mm	47.5	6.31 MPa
	Rib 2	0.0459 kg	0.0305 kg	32.6%	0.0044 mm	18.5	1.62 MPa
	Rib 3	0.042 kg	0.029 kg	31%	0.05 mm	38.9	0.77 MPa
	Rib 4	0.035 kg	0.026 kg	25.7%	0.094 mm	35.7	0.84 MPa
	Rib 5	0.031 kg	0.024 kg	22.6%	0.15 mm	30.7	0.98 MPa
	Rib 6	0.029 kg	0.026 kg	10.3%	2.07 mm	8.9	3.38 MPa
	Rib 7	0.033 kg	0.033 kg	0	0		0
Moving Wing	Rib 1	0.022 kg	0.012 kg	70.1%	0.0026 mm	38.8	0.078 MPa
	Rib 2	0.016 kg	0.01 kg	37.5%	0.00078 mm	310.9	0.097 MPa
	Rib 3	0.016 kg	0.01 kg	37.5%	0.00078 mm	310.9	0.097 MPa
	Rib 4	0.016 kg	0.01 kg	37.5%	0.00078 mm	310.9	0.079 MPa
	Rib 5	0.016 kg	0.01 kg	37.5%	0.00037 mm	68.6	0.032 MPa
	Rib 6	0.016 kg	0.01 kg	37.5%	0.00037 mm	68.6	0.027 MPa
	Rib 7	0.044 kg	0.044 kg	0	0		0

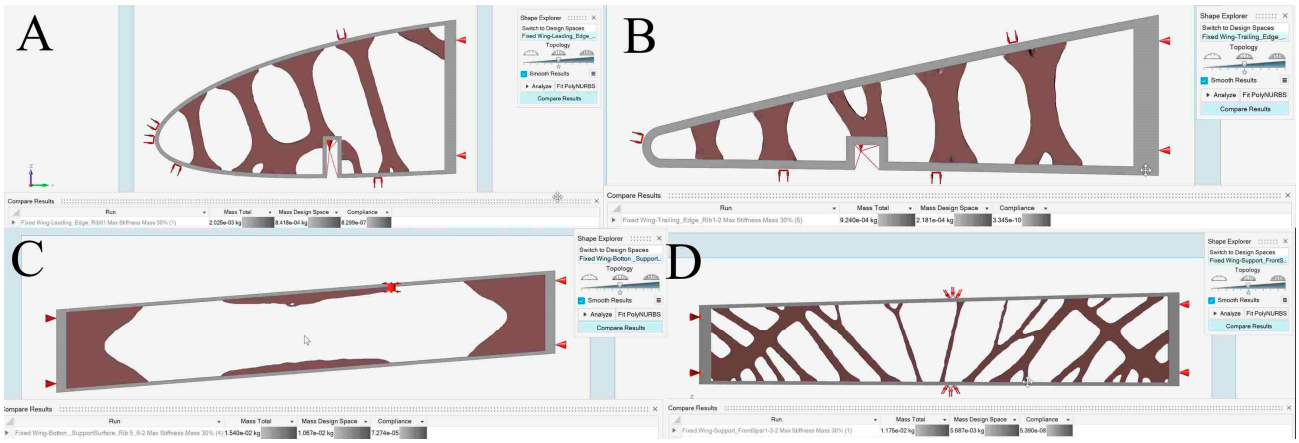

Figure 26. Variation in element density in relation to TO results of a fixed wing: (**A**) leading edge of rib 1, (**B**) trailing edge of rib 1, (**C**) bottom support surface between rib 6 and rib 7, and (**D**) front spar support.

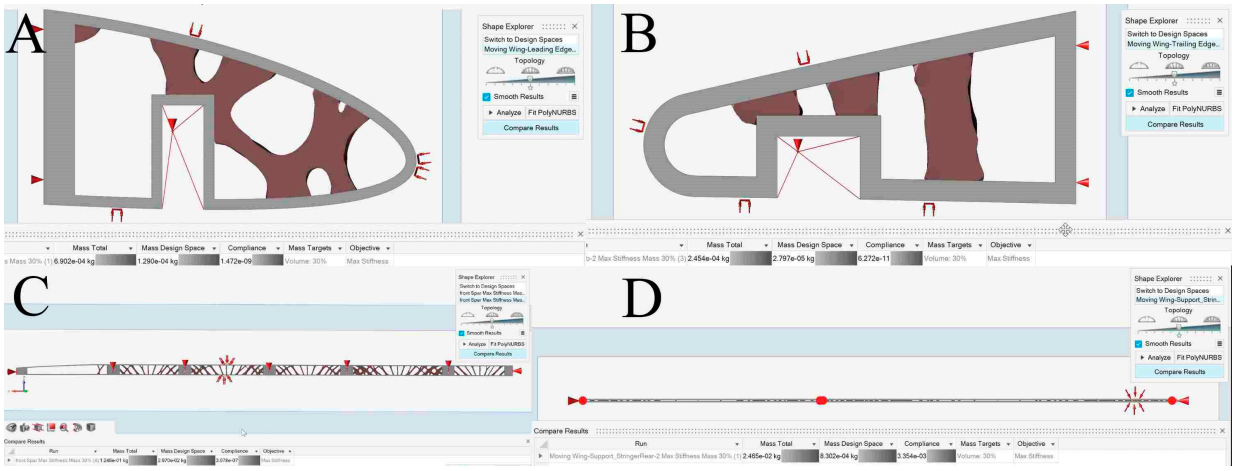

Figure 27. Variation in element density obtained using TO for a moving wing: (**A**) leading edge of rib 1, (**B**) trailing edge of rib 1, (**C**) support stringer of a front spar, and (**D**) support stringer of a rear spar.

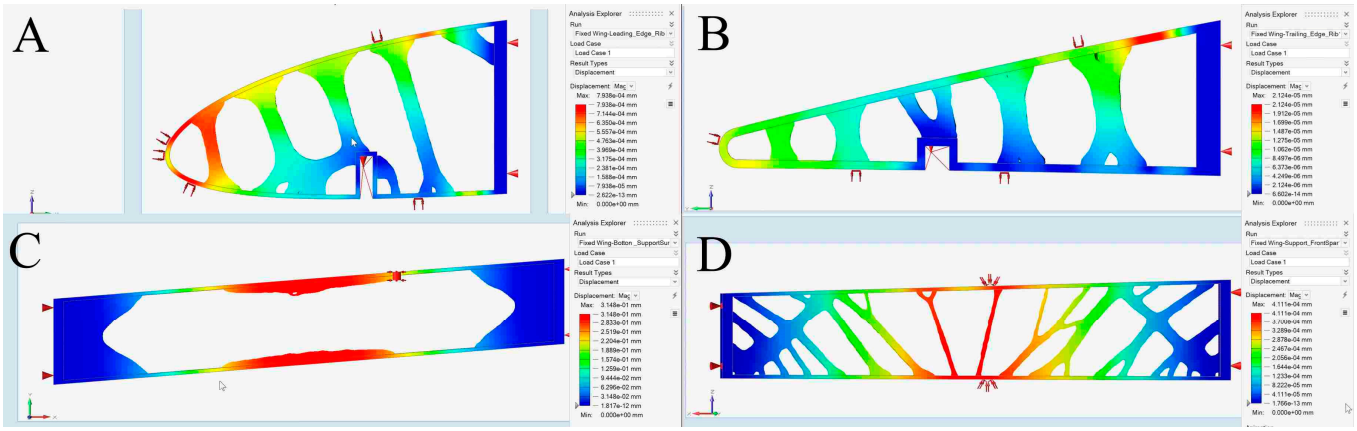

Figure 28. Displacement values in relation to topology optimization results of a fixed wing: (**A**) leading edge of rib 1, (**B**) trailing edge of rib 1, (**C**) bottom support surface between ribs 6 and 7, and (**D**) support of a front spar.

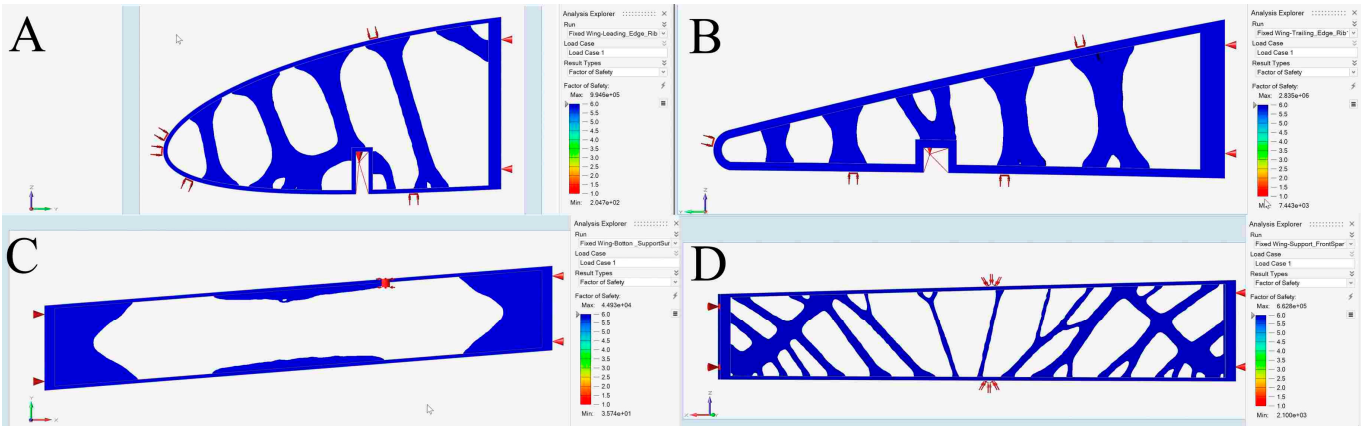

Figure 29. Safety factor evaluations obtained using TO for a fixed wing: (**A**) leading edge of rib 1, the (**B**) trailing edge of rib 1, (**C**) bottom support surface between ribs 6 and 7, and (**D**) support of a front spar.

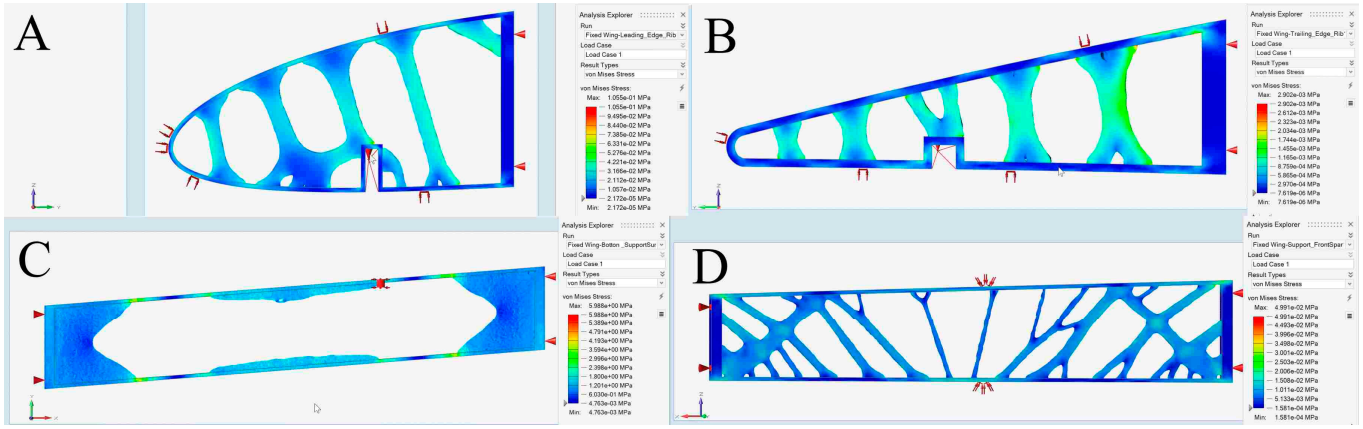

Figure 30. Von mises stress values obtained using TO for a fixed wing: (**A**) leading edge of rib 1, (**B**) trailing edge of rib 1, (**C**) bottom support surface between ribs 6 and 7, and (**D**) support of a front spar.

Based on the TO results, the fundamental structure of support components was substantially optimized by reducing the weights of the support elements. Furthermore, as

seen in Figure 29, structural compliance decreases as the number of iterations increases and does not affect the stiffness of the components.

Figures 31–33 illustrate the impacts of a TO method on structural changes in mechanical parameters for moving segment, such as deformations and stresses. These figures show that the strain can be minimized while structural stiffness increases progressively.

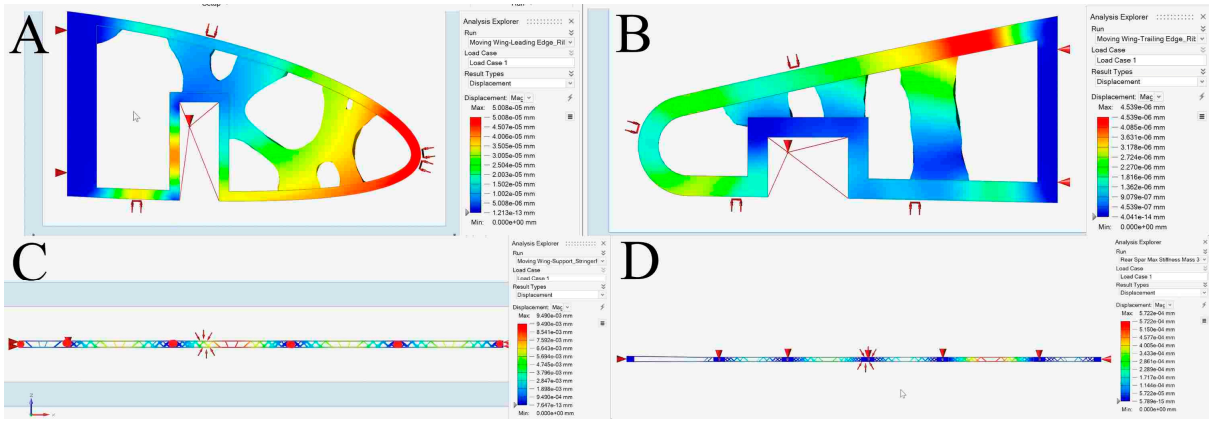

Figure 31. Displacement values obtained using TO for a moving wing: (**A**) leading edge of rib 1, (**B**) trailing edge of rib 1, (**C**) support stringer of a front spar, and (**D**) support stringer of a rear spar.

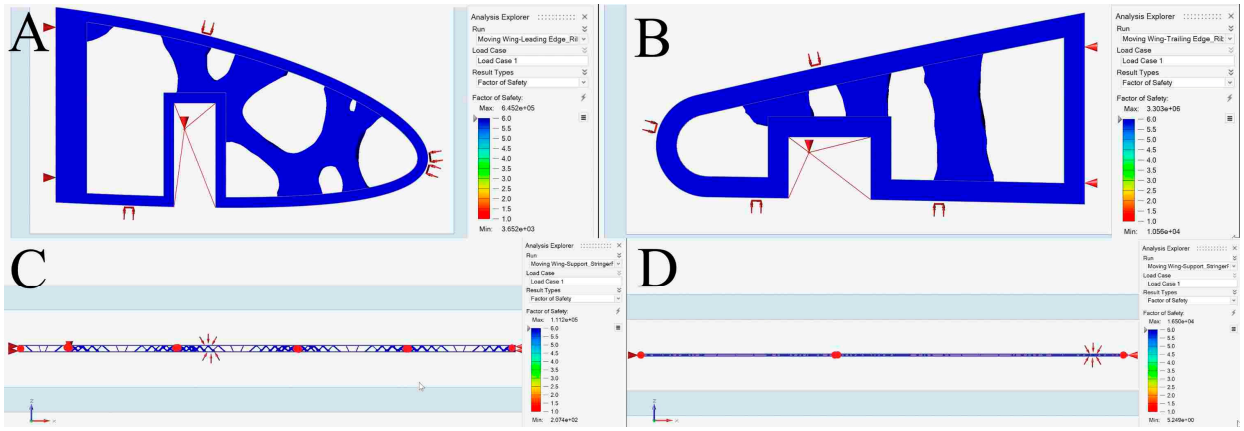

Figure 32. Safety factor evaluations obtained using TO for a moving wing: (**A**) leading edge of rib 1, (**B**) trailing edge of rib 1, (**C**) support stringer of a front spar, and (**D**) support stringer of a rear spar.

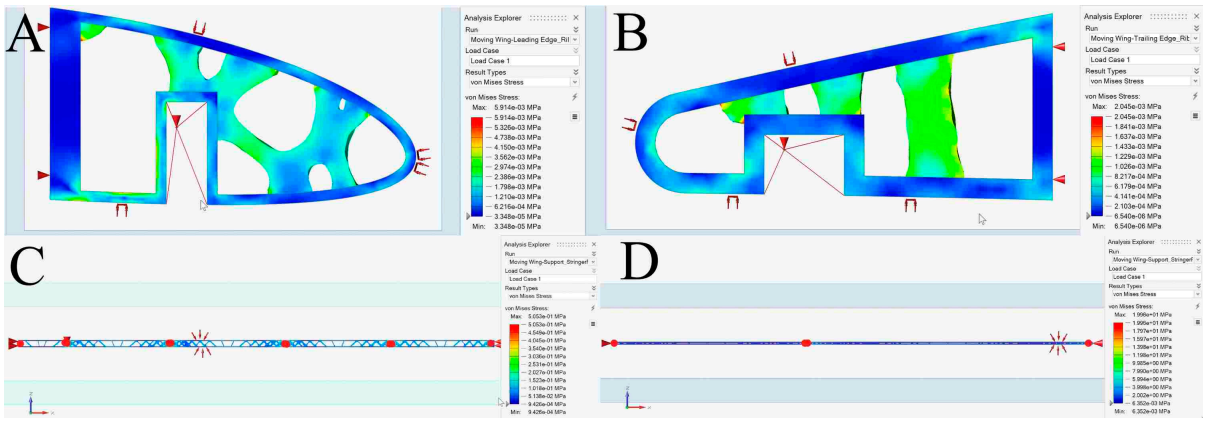

Figure 33. Von mises stress values obtained using TO for a moving wing: (**A**) leading edge of rib 1, (**B**) trailing edge of rib 1, (**C**) support stringer of a front spar, and (**D**) support stringer of a rear spar.

The values of the primary parameters obtained from the FEA were obtained as part of the optimization analysis. The optimization outputs varied according to the number of iterations and the type of mechanical investigation, and due to various loads and geometrical shapes of the support elements, they differed between each component of the support elements. A few support elements were eliminated from the optimization process due to geometrical and physical limitations, such as their cylindrical shape and small geometrical dimensions.

7. Performance Comparison between the Optimized VSMTW, the UAS-S4, and the Wing Components' Final Design

The morphing wing configuration is generally employed to complete numerous missions during a single flight. The study described in this article was conducted on Hydra Technologies' UAS-S4 [74]. First, the SO was used to determine the wing skin materials and then to calculate its optimal thickness. Then, the TO was used to establish the optimal internal wing components to minimize their weights while enhancing their structural stiffnesses. Finally, the wing component design configurations were evaluated based on the optimization results to determine which configuration should be the best to use. The optimization was conducted on both fixed and moving wings to allow the structure of the wing components to be redesigned and compared to a previous optimization of an aluminum alloy 2024-T3 wing [31]. The optimized wing model was designed using composite materials and specified for individual components such as spars and ribs. Table 13 compares the performances and weights of optimized wings made of composite materials, aluminum alloy 2024-T3, and the original UAS-S4 wing. The aerodynamic performance data in Table 13 were collected at sea level altitude and maximum speed.

Table 13. Comparison of optimized VSMTW and UAS-S4 wing in terms of aerodynamic performance and weight.

		Aerodynamic Performance			Weight
		Lift	Drag	L/D	
UAS-S4 wing		347.02 N	16.34 N	21.2	6.5 kg
VSMTW at full wing extension	Alu 2024-T3	1509.89 N	45.59 N	33.1	12.4 kg
	Composite material	1509.89 N	45.59 N	33.1	5.5 kg

Table 13 clearly shows that the VWTSW technique's performance outperforms substantially compared to the UAS-wing. However, the greatest challenge is reducing weight while enhancing wing strength. The results in Table 13 demonstrate that the optimized wing made of composite material fulfilled its weight reduction and performance objectives. The optimized wing made with aluminum 2024-T3 is heavier than the UAS-S4 wing and so should be modified to achieve the primary objective of designing a lightweight, strong wing. The majority of the weight is concentrated in the wing skin; the weight of the wing skin for both segments with aluminum is approximately 7.4 kg, while the wing skin for both segments with composite material weighs around 3.4 kg. Thus, based on the optimization method's data computation, the optimal wing with aluminum alloy 2024-T3 can be enhanced in terms of weight by replacing its skin with optimized skin of composite material. The wing segments with optimized internal components made with aluminum alloy 2024-T3 and optimized wing skin of composite materials weigh approximately 7.95 kg.

It is necessary to determine how the wing components are placed with respect to each other and then to build a frame model that accurately represents the final design. In this optimization part of the project, the TO approach was used for the wing components modeling, including the spars and ribs, similar to the previous TO work in this area [31]. Since certain support components were structurally inefficient, the TO technique was not applied to these support elements. The most challenging aspect of the optimization approach was undertaking TO on the fixed wing ribs. Each rib in the fixed wing was

assumed to have a cavity in the middle, as shown in Figure 8, to accommodate the moving wing. It was subsequently established that strengthening the fixed wing's center section would be necessary to boost the ribs in the impaired regions where the moving wing's motion generated substantially. Because of the shear stress generated by the aerodynamic loads' reactions in a range of flight conditions, both wing segments had to be strengthened. The CAD model for the MVSTW components was built using the density distribution of the wing segments after TO results. Figure 34 shows the optimal structures for both wing segments.

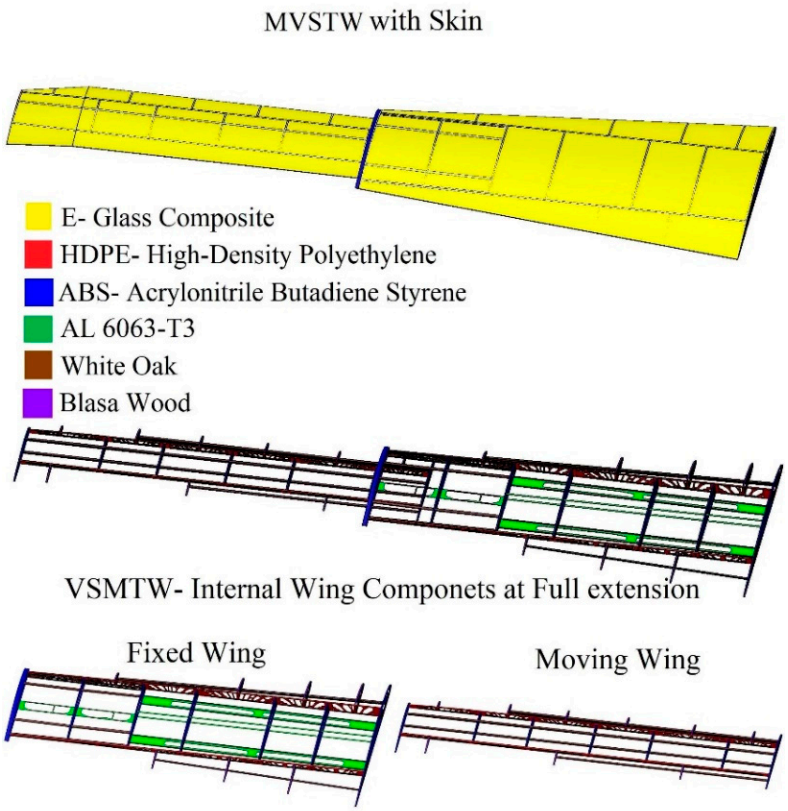

Figure 34. MVSTW remodeled in detail, using composite materials for its components.

After incorporating the optimized components' structural configuration data into the overall design, the weights of the enhanced wing components were reduced to 2.13 kg for the fixed section and to 1.22 kg for the moving segment. As a result, the entire MVSTW was roughly 1 kg smaller than the original UAS-S4 wing weight.

8. Conclusions

This article discusses the progress in incorporating multidisciplinary optimization methodologies simultaneously to optimize and develop the concept of the morphing variable span of a tapered wing (MVSTW) using composite materials. The novel wing component optimization involved merging multi-codes of aerodynamic optimization, material selection, sizing, and topology optimization. The MATLAB algorithm was used to determine the most appropriate composite materials. Altair's OptiStruct and SolidThinking Inspire solvers were then utilized to perform both the size and topology optimizations. Both solvers' outputs were linked to the aerodynamic analysis results generated by ANSYS Fluent and XFLR5 code using CFD. The primary purpose of this investigation was to specify and evaluate the feasibility of executing these multi-optimization methods on the skin and interior wing components using certain composite materials.

The objective of this study was to reduce the weight of the MVSTW while increasing its global stiffness to improve structural durability accordingly to MVSTW's structural

integrity standards. The STO results indicated that employing composite materials resulted in structural weight reduction when comparing an optimized wing with the UAS-S4 wing, and thus in a significant improvement in aerodynamic performance. The optimized wing components' weights for both segments were reduced to 2.13 kg for the fixed wing and to 1.22 kg for the moving wing. Based on the optimization outcomes for both MVSTW components, the redesigns of the wing components, comprising spars, ribs, and support elements, were modified using MATLAB code to determine the appropriate material for each type of component and were further developed. For example, E-glass was chosen for the skin, and its weight has been decreased by roughly 80%, while HDPE was chosen for the spars, and the findings reveal a weight reduction of up to 41%. Similar methodologies were considered for the ribs, and the ABS material was used; their weight reduction ranged between 10% and 70%. The support elements were designed from Al 6063-T3, white oak, and balsa wood, and the results displayed the same pattern as the other components.

Additional research will be undertaken in future work to advance the development of an adaptive morphing wing. The MVSTW arrangement will be integrated with an actuation mechanism and evaluated after the wing segments' optimization utilizing composite materials. The final design of the MVSTW, which was obtained through an optimization process and then integrated with an actuation system, will be manufactured as a prototype for experimental wind tunnel tests.

Author Contributions: M.E. carried out the research presented in this paper, methodology, investigation, design, and the modeling of the MVSTW with CATIA, XFLR5, and HyperMesh software. F.S.P. carried out the material selection using MATLAB code participated in the writing of the research paper. Review and editing were by R.M.B. and T.-M.D. All authors have read and agreed to the published version of the manuscript.

Funding: This research received no external funding.

Institutional Review Board Statement: Not applicable.

Informed Consent Statement: Not applicable.

Data Availability Statement: The data presented in this study are available on request from the corresponding author.

Acknowledgments: Special thanks are due to the Natural Sciences and Engineering Research Council of Canada (NSERC) for funding the Canada Research Tier 1 in Aircraft Modeling and Simulation Technologies. Additionally, we would like to express our gratitude to Odette Lacasse and Oscar Carranza for their support at the ETS, as well as to the Hydra Technologies team members in Mexico, Carlos Ruiz, Eduardo Yakin, and Alvaro Gutierrez Prado for their collaboration.

Conflicts of Interest: The authors declare no conflict of interest.

Nomenclature

A	Laminate extension stiffness matrix
ABS	Acrylonitrile Butadiene Styrene
B	Laminate coupling stiffness matrix
CAE	Computer-Aided Engineering
CFD	Computational Fluid Dynamics
D	Laminate bending stiffness matrix
E_1	Lamina longitudinal Young's modulus
E_2	Transverse Young's modulus
E_{f1}	The longitudinal Young's modulus of the fiber
E_m	The longitudinal Young's modulus of the matrix
$E_{(xi)}$	Young's modulus of each element
E_{solid}	Young's modulus of solid regions
E_{void}	Very low Young's modulus
E_x	Longitudinal Young's modulus
E_y	Transversal Young's

f	Distributed body force
F	Force vector
FAA	Federal Aviation Regulations
FEM	Finite Element Method
Fi	Point load on the ith node
FRPs	Fiber-reinforced plastics
HDPE	High-Density Polyethylene
G_{xy}	Shear modulus
K	Global stiffness matrix
k_0	Elemental stiffness matrix
MDO	Multidisciplinary optimization
MVSTW	Morphing Variable Span of Tapered Wing
S	Surface area of the continuum
SIMP	Solid Isotropic Material with the Penalization
t	Traction force
TO	Topology Optimization
u	Displacement area
U	Global displacement
UAVs	Unmanned Aerial Vehicles
Ui	ith displacement degree of freedom
V	Total volume
v_f	The volume fractions of the fiber
v_m	The volume fractions of the fiber and the matrix
V_0	Initial volume
V_i	Volume of the ith element
V_{xy}	Poisson's ratio
$\Gamma_{(y)}$	Circulation distribution
Xi	Pseudo density
ρ_0	Density of the base material

References

1. Judge, J.F. Composite materials—The coming revolution (Filamentary composite materials for commercial aircraft and engine construction noting boron, graphite and glass reinforcement). *Airl. Manag. Mark. Incl. Am. Aviat.* **1969**, *1*, 85.
2. Concilio, A.; Dimino, I.; Pecora, R. SARISTU: Adaptive Trailing Edge Device (ATED) design process review. *Chin. J. Aeronaut.* **2021**, *34*, 187–210. [CrossRef]
3. Pecora, R.; Barbarino, S.; Concilio, A.; Lecce, L.; Russo, S. Design and functional test of a morphing high-lift device for a regional aircraft. *J. Intell. Mater. Syst. Struct.* **2011**, *22*, 1005–1023. [CrossRef]
4. Dimino, I.; Lecce, L.; Pecora, R. *Morphing Wing Technologies: Large Commercial Aircraft and Civil Helicopters*; Butterworth-Heinemann: Oxford, UK, 2017.
5. Rajak, D.K.; Pagar, D.D.; Kumar, R.; Pruncu, C.I. Recent progress of reinforcement materials: A comprehensive overview of composite materials. *J. Mater. Res. Technol.* **2019**, *8*, 6354–6374. [CrossRef]
6. Rajak, D.K.; Pagar, D.D.; Menezes, P.L.; Linul, E. Fiber-reinforced polymer composites: Manufacturing, roperties, and applications. *Polymers* **2019**, *11*, 1667. [CrossRef]
7. Jerome, P. Composite materials in the airbus A380-from history to future. In Proceedings of the Beijing: Proceedings 13th International Conference on Composite Materials (ICCM-13), Beijing, China, 25–29 June 2001.
8. Aamir, M.; Tolouei-Rad, M.; Giasin, K.; Nosrati, A. Recent advances in drilling of carbon fiber–reinforced polymers for aerospace applications: A review. *Int. J. Adv. Manuf. Technol.* **2019**, *105*, 2289–2308. [CrossRef]
9. Dillinger, J.; Klimmek, T.; Abdalla, M.M.; Gürdal, Z. Stiffness optimization of composite wings with aeroelastic constraints. *J. Aircr.* **2013**, *50*, 1159–1168. [CrossRef]
10. Guo, S. Aeroelastic optimization of an aerobatic aircraft wing structure. *Aerosp. Sci. Technol.* **2007**, *11*, 396–404. [CrossRef]
11. Sullivan, J.M. Evolution or revolution? The rise of UAVs. *IEEE Technol. Soc. Mag.* **2006**, *25*, 43–49. [CrossRef]
12. Arena, M.; Concilio, A.; Pecora, R. Aero-servo-elastic design of a morphing wing trailing edge system for enhanced cruise performance. *Aerosp. Sci. Technol.* **2019**, *86*, 215–235. [CrossRef]
13. Botez, R.M.; Grigorie, T.L.; Khan, S.; Mamou, M.; Mebarki, Y. A smart controlled morphing wing experimental model with the structure based on a full-scaled portion of a real wing. In Proceedings of the AIAA Scitech 2021 Forum, Virtual Event, 11–15 & 19–21 January 2021; p. 1836.

14. Botez, R.M.; Koreanschi, A.; Gabor, O.S.; Tondji, Y.; Guezguez, M.; Kammegne, J.T.; Grigorie, L.T.; Sandu, D.; Mebarki, Y.; Mamou, M.; et al. Numerical and experimental transition results evaluation for a morphing wing and aileron system. *Aeronaut. J.* **2018**, *122*, 747–784. [CrossRef]
15. Concilio, A.; Dimino, I.; Pecora, R.; Ciminello, M. Structural design of an adaptive wing trailing edge for enhanced cruise performance. In Proceedings of the 24th AIAA/AHS Adaptive Structures Conference, San Diego, CA, USA, 4–8 January 2016; p. 1317.
16. Dimino, I.; Andreutti, G.; Moens, F.; Fonte, F.; Pecora, R. Integrated Design of a Morphing Winglet for Active Load Control and Alleviation of Turboprop Regional Aircraft. *Appl. Sci.* **2021**, *11*, 2439. [CrossRef]
17. Mieloszyk, J.; Tarnowski, A.; Kowalik, M.; Perz, R.; Rzadkowski, W. Preliminary design of 3D printed fittings for UAV. *Aircr. Eng. Aerosp. Technol.* **2019**, *91*, 756–760. [CrossRef]
18. Easter, S.; Turman, J.; Sheffler, D.; Balazs, M.; Rotner, J. Using advanced manufacturing to produce unmanned aerial vehicles: A feasibility study. In *Ground/Air Multisensor Interoperability, Integration, and Networking for Persistent ISR IV*; International Society for Optics and Photonics: Bellingham, WC, USA, 2013; Volume 8742, p. 874204.
19. Dimino, I.; Flauto, D.; Diodati, G.; Pecora, R. Actuation system design for a morphing wing trailing edge. *Recent Pat. Mech. Eng.* **2014**, *7*, 138–148. [CrossRef]
20. Rathod, V.T.; Kumar, J.S.; Jain, A. Polymer and ceramic nanocomposites for aerospace applications. *Appl. Nanosci.* **2017**, *7*, 519–548. [CrossRef]
21. Setlak, L.; Kowalik, R. Examination of multi-pulse rectifiers of PES systems used on airplanes compliant with the concept of electrified aircraft. *Appl. Sci.* **2019**, *9*, 1520. [CrossRef]
22. Setlak, L.; Kowalik, R.; Lusiak, T. Practical Use of Composite Materials Used in Military Aircraft. *Materials* **2021**, *14*, 4812. [CrossRef]
23. Locatelli, D.; Mulani, S.B.; Kapania, R.K. Parameterization of curvilinear spars and ribs for optimum wing structural design. *J. Aircr.* **2014**, *51*, 532–546. [CrossRef]
24. Wang, W.; Guo, S.; Yang, W. Simultaneous partial topology and size optimization of a wing structure using ant colony and gradient based methods. *Eng. Optim.* **2011**, *43*, 433–446. [CrossRef]
25. Stanford, B.K.; Jutte, C.V.; Coker, C.A. Aeroelastic Sizing and Layout Design of a Wingbox Through Nested Optimization. *AIAA J.* **2019**, *57*, 848–857. [CrossRef]
26. Grihon, S.; Krog, L.; Hertel, K. A380 weight savings using numerical structural optimization. In Proceedings of the 20th AAAF Colloqium "Material for Aerospace Application", Paris, France, 9–12 November 2004.
27. Wang, Q.; Lu, Z.; Zhou, C. New Topology Optimization Method for Wing Leading-Edge Ribs. *J. Aircr.* **2011**, *48*, 1741–1748. [CrossRef]
28. James, K.A.; Kennedy, G.J.; Martins, J.R.R.A. Concurrent aerostructural topology optimization of a wing box. *Comput. Struct.* **2014**, *134*, 1–17. [CrossRef]
29. Botez, R.M. Overview of Morphing Aircraft and Unmanned Aerial Systems Methodologies and Results–Application on the Cessna Citation X, CRJ-700, UAS-S4 and UAS-S45. In Proceedings of the AIAA SCITECH 2022 Forum, San Diego, CA, USA, 3–7 January 2022; p. 1038.
30. Botez, R. Morphing wing, UAV and aircraft multidisciplinary studies at the Laboratory of Applied Research in Active Controls, Avionics and AeroServoElasticity LARCASE. *Aerosp. Lab* **2018**, 1–11. [CrossRef]
31. Elelwi, M.; Botez, R.M.; Dao, T.-M. Structural Sizing and Topology Optimization Based on Weight Minimization of a Variable Tapered Span-Morphing Wing for Aerodynamic Performance Improvements. *Biomimetics* **2021**, *6*, 55. [CrossRef]
32. Kammegne, M.J.T.; Botez, R.M.; Grigorie, T.L.; Manou, M.; Mebarki, Y. A fuel saving way in aerospace engineering based on morphing wing technology: A new multidisciplinary experimental model. *Int. J. Contemp. Energy* **2016**, *2*, 2016. (In English) [CrossRef]
33. Botez, R.M.; Molaret, P.; Laurendeau, E. Laminar flow control on a research wing project presentation covering a three year period. In Proceedings of the Canadian Aeronautics and Space Institute Annual General Meeting, Toronto, ON, Canada, 30 April–2 May 2007; Volume 2007.
34. Noviello, M.C.; Dimino, I.; Amoroso, F.; Pecora, R. Aeroelastic assessments and functional hazard analysis of a regional aircraft equipped with morphing winglets. *Aerospace* **2019**, *6*, 104. [CrossRef]
35. Elelwi, M.; Kuitche, M.A.; Botez, R.M.; Dao, T.M. Comparison and analyses of a variable span-morphing of the tapered wing with a varying sweep angle. *Aeronaut. J.* **2020**, *124*, 1146–1169. [CrossRef]
36. Zhu, J.-H.; Zhang, W.-H.; Xia, L. Topology Optimization in Aircraft and Aerospace Structures Design. *Arch. Comput. Methods Eng.* **2016**, *23*, 595–622. [CrossRef]
37. Elelwi, M.; Calvet, T.; Botez, R.M.; Dao, T.M. Wing component allocation for a morphing variable span of tapered wing using finite element method and topology optimisation—Application to the UAS-S4. *Aeronaut. J.* **2021**, *125*, 1313–1336. [CrossRef]
38. Pecora, R. Morphing wing flaps for large civil aircraft: Evolution of a smart technology across the Clean Sky program. *Chin. J. Aeronaut.* **2021**, *34*, 13–28. [CrossRef]
39. Sugar-Gabor, O. Nonlinear lifting-line model using a vector formulation of the unsteady Kutta-Joukowski theorem. *INCAS Bull.* **2019**, *11*, 189–203. [CrossRef]
40. Zhang, Q.; Liu, H.H.T. Aerodynamics Modeling and Analysis of Close Formation Flight. *J. Aircr.* **2017**, *54*, 2192–2204. [CrossRef]

41. Gross, A.; Fasel, H.F.; Gaster, M. Criterion for Spanwise Spacing of Stall Cells. *AIAA J.* **2015**, *53*, 272–274. [CrossRef]
42. Acar, E.; Haftka, R.T.; Kim, N.H. Effects of structural tests on aircraft safety. *AIAA J.* **2010**, *48*, 2235–2248. [CrossRef]
43. Shokrieh, M.M.; Moshrefzadeh-Sani, H. On the constant parameters of Halpin-Tsai equation. *Polymer* **2016**, *106*, 14–20. [CrossRef]
44. Gibson, R.F. *Principles of Composite Material Mechanics*; CRC Press: Boca Raton, FL, USA, 2016.
45. Degertekin, S.O.; Lamberti, L.; Ugur, I.B. Discrete sizing/layout/topology optimization of truss structures with an advanced Jaya algorithm. *Appl. Soft Comput.* **2019**, *79*, 363–390. [CrossRef]
46. Bendsøe, M.P. Optimal shape design as a material distribution problem. *Struct. Optim.* **1989**, *1*, 193–202. [CrossRef]
47. Assimi, H.; Jamali, A.; Nariman-Zadeh, N. Sizing and topology optimization of truss structures using genetic programming. *Swarm Evol. Comput.* **2017**, *37*, 90–103. [CrossRef]
48. Gunwant, D.; Misra, A. Topology Optimization of Sheet Metal Brackets Using ANSYS. *MIT Int. J. Mech. Eng.* **2012**, *2*, 120–126.
49. Aage, N.; Andreassen, E.; Lazarov, B.S.; Sigmund, O. Giga-voxel computational morphogenesis for structural design. *Nature* **2017**, *550*, 84–86. [CrossRef]
50. Bendsøe, M.P.; Sigmund, O. Material interpolation schemes in topology optimization. *Arch. Appl. Mech.* **1999**, *69*, 635–654. [CrossRef]
51. Höke, Ö.; Bozca, M. Topology Optimisation of Engine Cross Members for Lightweight Structure in Light Commercial Vehicles. *Int. J. Precis. Eng. Manuf.* **2020**, *21*, 465–482. [CrossRef]
52. Bakhtiarinejad, M. *Topology Optimization Based on Morphing Mesh for Simultaneous Component Relocation and Frame Structure Design*; University of Maryland: Baltimore, MD, USA, 2015.
53. Daynes, S.; Feih, S.; Lu, W.F.; Wei, J. Optimisation of functionally graded lattice structures using isostatic lines. *Mater. Des.* **2017**, *127*, 215–223. [CrossRef]
54. Mou, B.; He, B.-J.; Zhao, D.-X.; Chau, K.-W. Numerical simulation of the effects of building dimensional variation on wind pressure distribution. *Eng. Appl. Comput. Fluid Mech.* **2017**, *11*, 293–309. [CrossRef]
55. Vasista, S.; de Gaspari, A.; Ricci, S.; Riemenschneider, J.; Monner, H.P.; van de Kamp, B. Compliant structures-based wing and wingtip morphing devices. *Aircr. Eng. Aerosp. Technol. Int. J.* **2016**, *88*, 311–330. [CrossRef]
56. Gibson, R.F.; Plunkett, R. Dynamic mechanical behavior of fiber-reinforced composites: Measurement and analysis. *J. Compos. Mater.* **1976**, *10*, 325–341. [CrossRef]
57. Coroian, A.; Lupea, I. Improving the Sound Pressure Level for a Simplified Passenger Cabin by using Modal Participation and Size Optimization. *Rom. J. Acoust. Vib.* **2013**, *10*, 47–53.
58. Rinku, A.; Ananthasuresh, G. Topology and Size Optimization of Modular Ribs in Aircraft Wings. In Proceedings of the 11th World Congress on Structural and Multidisciplinary Optimisation, Sydney, Australia, 7–12 June 2015.
59. Girennavar, M.; Soumya, H.; Subodh, H.; Heraje, T.J.; Py, D.R. Design, Analysis and Testing of Wing Spar for Optimum Weight. *Int. J. Res. Sci. Innov.* **2017**, *4*, 104–112.
60. Batista, N.L.; Helal, E.; Kurusu, R.S.; Moghimian, N.; David, E.; Demarquette, N.R.; Hubert, P. Mass-produced graphene—HDPE nanocomposites: Thermal, rheological, electrical, and mechanical properties. *Polym. Eng. Sci.* **2019**, *59*, 675–682. [CrossRef]
61. Costa, I.L.M.; Zanini, N.C.; Mulinari, D.R. Thermal and Mechanical Properties of HDPE Reinforced with Al_2O_3 Nanoparticles Processed by Thermokinectic Mixer. *J. Inorg. Organomet. Polym. Mater.* **2021**, *31*, 220–228. [CrossRef]
62. Vasconcelos, G.d.C.; Basso, B.B.; Valera, T.S. Effect of impurity content on long term performance of recycled HDPE for structural application. *AIP Conf. Proc.* **2019**, *2065*, 040005. [CrossRef]
63. Awad, A.H.; el Gamasy, R.; el Wahab, A.A.; Abdellatif, M.H. Mechanical and Physical Properties of PP and HDPE. *Eng. Sci.* **2019**, *4*, 34–42. [CrossRef]
64. Contino, M.; Andena, L.; la Valle, V.; Rink, M.; Marra, G.; Resta, S. A comparison between K $ K $ and G $ G $ approaches for a viscoelastic material: The case of environmental stress cracking of HDPE. *Mech. Time-Depend. Mater.* **2020**, *24*, 381–394. [CrossRef]
65. Grbović, A.; Kastratović, G.; Sedmak, A.; Balać, I.; Popović, M.D. Fatigue crack paths in light aircraft wing spars. *Int. J. Fatigue* **2019**, *123*, 96–104. [CrossRef]
66. Grisval, J.-P.; Liauzun, C. Application of the finite element method to aeroelasticity. *Rev. Eur. Des Éléments Finis* **1999**, *8*, 553–579. [CrossRef]
67. Li, C.; Kim, I.Y.; Jeswiet, J. Conceptual and detailed design of an automotive engine cradle by using topology, shape, and size optimization. *Struct. Multidiscip. Optim.* **2015**, *51*, 547–564. [CrossRef]
68. Nomani, J.; Wilson, D.; Paulino, M.; Mohammed, M.I. Effect of layer thickness and cross-section geometry on the tensile and compression properties of 3D printed ABS. *Mater. Today Commun.* **2020**, *22*, 100626. [CrossRef]
69. Cantrell, J.; Rohde, S.; Damiani, D.; Gurnani, R.; DiSandro, L.; Anton, J.; Young, A.; Jerez, A.; Steinbach, D.; Kroese, C.; et al. Experimental Characterization of the Mechanical Properties of 3D Printed ABS and Polycarbonate Parts. In *Advancement of Optical Methods in Experimental Mechanics*; Springer International Publishing: Cham, Switzerland, 2017; Volume 3, pp. 89–105.
70. Sadler, R.L.; Sharpe, M.; Panduranga, R.; Shivakumar, K. Water immersion effect on swelling and compression properties of Eco-Core, PVC foam and balsa wood. *Compos. Struct.* **2009**, *90*, 330–336. [CrossRef]
71. Borrega, M.; Gibson, L.J. Mechanics of balsa (*Ochroma pyramidale*) wood. *Mech. Mater.* **2015**, *84*, 75–90. [CrossRef]
72. Erchiqui, F.; Annasabi, Z.; Diagne, M. Investigation of the radiofrequency heating of anisotropic dielectric materials with a phase change: Application to frozen Douglas-fir and white oak woods. *Wood Sci. Technol.* **2022**, *56*, 259–283. [CrossRef]

73. Singh, A.; Agrawal, A. Investigation of surface residual stress distribution in deformation machining process for aluminum alloy. *J. Mater. Processing Technol.* **2015**, *225*, 195–202. [CrossRef]
74. Kuitche, M.A.J.; Botez, R.M. Modeling novel methodologies for unmanned aerial systems—Applications to the UAS-S4 Ehecatl and the UAS-S45 Bálaam. *Chin. J. Aeronaut.* **2019**, *32*, 58–77. [CrossRef]